Review

Review of elastic light scattering from single aerosol particles and application in bioaerosol detection

Yong-Le Pan[a,*], Kevin Aptowicz[b], Jessica Arnold[a], Samuel Cheng[a,c], Aimable Kalume[a], Patricio Piedra[a], Chuji Wang[d], Joshua Santarpia[e], Gorden Videen[a,f,g]

[a] CCDC-US Army Research Laboratory, Adelphi, MD 20783, United States
[b] Department of Physics and Engineering, West Chester University, West Chester, PA 19383, United States
[c] Centennial High School, Ellicott City, MD 21042, United States
[d] Department of Physics and Astronomy, Mississippi State University, Starkville, MS 39759, United States
[e] National Strategic Research Institute and University of Nebraska Medical Center, Omaha, NE, 68198, United States
[f] Space Science Institute, 4750 Walnut Street, Boulder Suite 205, CO 80301, United States
[g] Department of Astronomy and Space Science, Kyung Hee University, 1732, Deogyeong-daero, Giheung-gu, Yongin-si, Gyeonggi-do 17104, South Korea

A R T I C L E   I N F O

A B S T R A C T

Elastic light scattering (ELS) from single micron-sized particles has been used as a fast, non-destructive diagnostic tool in life science, physics, chemistry, climatology, and astrophysics. Due to the large scattering cross-section, ELS can be used to find trace amounts of suspect particles such as bioaerosols among complex, diverse atmospheric aerosols, based on single-particle interrogation. In this article, we briefly summarized the main computational models and instrumentation developed for ELS, then reviewed how properties like particle size, refractive index, degree of symmetry, and surface roughness, in addition to packing density, shape of primary particles in an aggregate, and special helix structures in compositions can be determined from ELS measurements. Meanwhile, we emphasize on how these parameters obtained from ELS measurements can be used for bioaerosol detection, characterization, and discrimination from atmospheric aerosol particles using different classification algorithms.

1. Introduction

The rapid detection and characterization of aerosol particles, especially the potential threat from aerosolized biological hazards/agents, such as the novel coronavirus in the COVID-19 pandemic, has become increasingly important since 9/11. This demand has motivated significant, relevant, fundamental research, and the development of corresponding technologies [74,127]. Real-time detection and characterization of aerosol particles are often based on detecting chemical signatures, for instance, using mass spectroscopy, breakdown/ plasma spectroscopy, fluorescence spectroscopy, gas-chromatography-ion mobility spectrometry, absorption spectroscopy, or Raman spectroscopy [74,127]. In general, each of these technologies can reveal one or a few particular properties, then provide information from an orthogonal viewpoint for the target aerosol particles among the extremely

complex mixture of atmospheric aerosol particles. Laser-induced fluorescence spectroscopy can reveal the electronic, rovibrational states of molecules within the particles and has been used as the main bioaerosol early warning system. Plasma or breakdown spectroscopy (e.g. laser-induced-breakdown spectroscopy) and X-ray fluorescence spectroscopy can provide elemental compositions of the particles, while mass spectroscopy is more widely used in chemical analyses for their elemental compositions and molecular fragments of the particles. Infrared absorption and Raman spectroscopy provide rotational and vibrational information of molecular compositions. Biochemical analyses have demonstrated the ability to identify bioaerosol particles, but generally require a relatively large number of samples, expensive analytical reagents, and/or prolonged diagnostic times. These make rapid, *in situ* analysis problematic (e.g. [74,127]). ELS and imaging from optical, atomic force, digital holographic, and electron microscopes can supplement these technologies by providing particle size and morphology information directly.

Many bioaerosol point-detection systems are based on rapid measurements from single aerosol particles when they are succes-

* Corresponding author at: US Army Research Laboratory, 2800 Powder Mill Rd, Adelphi, MD 20783, United States.
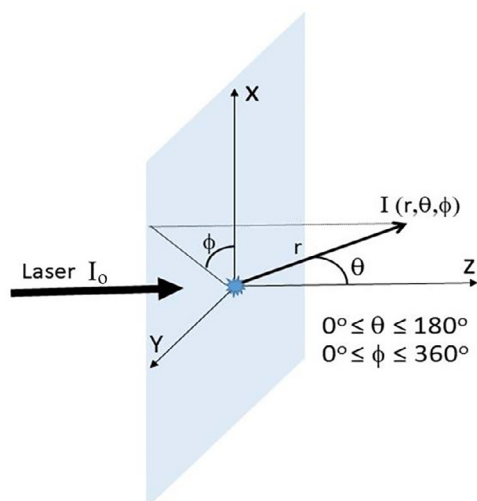*E-mail address:* yongle.pan.civ@army.mil (Y.-L. Pan).

Fig. 1. Spherical coordinates for describing optical light scattering.

sively drawn through an interrogation volume (e.g. [74]). An advantage of single-particle, on-line analyses is the capability to detect target bioaerosol particles at low concentration contained within a large number of other atmospheric aerosol particles. Remote systems, like lidar, have the advantage of being able to gather information at a distance while interrogating a large volume of the atmospheric aerosol particles. However, a disadvantage of lidar is if the targeted aerosol is nestled within a volume containing other benign aerosols, the signal from the other aerosols can swamp the signal of interest and make the detection of the potential threat more challenging (e.g. [19]).

Comparing the quantum efficiencies, or optical cross sections among these different technologies, ELS has the highest sensitivity in obtaining information for aerosol characterization, such as bioaerosol detection, via single-particle or multiple particle interrogation (e.g. [31,71,81,107,113,116,129]). ELS changes the spatial distribution and/or propagation direction of the illuminating light, without modification of the photon energy, which occurs for inelastic scattering processes like laser-induced fluorescence and Raman scattering. Generally, the spherical coordinate system is used to describe the ELS, where light illumination with intensity I_o propagates along the z-axis. The scattered light intensity $I (r, \theta, \phi)$ is designated at a point in spherical coordinates as shown in Fig. 1.

For large kr, where $k = 2\pi/\lambda$ is the wavenumber, and λ is the incident wavelength, the far-field intensity distribution of the scattered light is conveniently represented as:

$$I(r, \theta, \varphi) = (kr)^{-2} P(\theta, \varphi) I_o \tag{1}$$

where $P(\theta, \phi)$ is the relative intensity distribution from the scattering particle. Prior to the development of the CCD, this two-dimensional scattering function could be captured by placing a photographic plate or sheet in the far field. Note that if polarization is considered, the quantities $I (r, \theta, \phi)$ and I_o represent the scattered and incident Stokes vectors, respectively, and $P(\theta, \phi)$ represents the ELS Mueller matrix.

To write I into the Stokes vector format, the polarization state of a light beam can be completely described by the four parameters as [75],

$$S = \begin{bmatrix} I \\ Q \\ U \\ V \end{bmatrix} = \begin{bmatrix} I_\perp + I_\parallel \\ I_\perp - I_\parallel \\ I_{+45} - I_{-45} \\ I_R - I_L \end{bmatrix} \tag{2}$$

Given an input beam S_{in}, the output beam S_{out} after interacting with an optical or scattering objective can be determined by operating a 4 × 4 Mueller matrix (e.g. [24]) describing the optical system as M:

$$S_{out} = M \times S_{in}, or$$

$$\begin{bmatrix} I_{out} \\ Q_{out} \\ U_{out} \\ V_{out} \end{bmatrix} = \begin{bmatrix} S_{11} & S_{12} & S_{13} & S_{14} \\ S_{21} & S_{22} & S_{23} & S_{24} \\ S_{31} & S_{32} & S_{33} & S_{34} \\ S_{41} & S_{42} & S_{43} & S_{44} \end{bmatrix} \times \begin{bmatrix} I_{in} \\ Q_{in} \\ U_{in} \\ V_{in} \end{bmatrix} \tag{3}$$

Experimentally, the Stokes vector S is measurable directly. The Mueller matrix characterizes the scatterer in a particular orientation. While the S_{11} matrix element (total scattering intensity I) can be determined from a single measurement, other elements require multiple measurements of the scattered Stokes vector [18], which can be performed simultaneously through the ingenious method of polarization modulation [75]. Numerous studies have shown that the full or partial Mueller matrix, which contains both intensity and polarization information, can supply more signatures for the characterization of scattering aerosol particles [18,20,24,75,76,110,116,123,138,139]. In general, the ELS characteristics contained in M are determined by the size, shape and chemistry of the scattering particle. It also depends on particle orientation relative to the illuminating light. The chemical properties are contained in the complex refractive index of the particle $n = n_r + in_i$, where n_r and n_i are the real and imaginary parts. Most studies assume the refractive index is homogeneous, although this approximation is not always a good one for heterogeneous particles [37]. While M is determined by the properties of the ELS system, it should be emphasized that in many cases the signal is not unique; i.e., different particle systems can produce the same M. This is especially true for complex particle systems [202]. It means that it may be difficult to obtain information about a particle system without having some *a priori* information. In another words, it is still a big challenge to retrieve the properties or parameters of a particle from its ELS measurements. In this review, we will mainly focus on studies related to the ELS from single aerosol particles, particularly in the application of bioaerosol detection of micron-sized particles.

2. Theoretical models for light scattering

ELS studies of atmospheric constituents can be traced back as early as the 17th century when Descartes [41] tried to explain the nature of the rainbow. Since then, researchers have undertaken thousands of investigations to characterize the atmosphere, including characterizing pollutants, determining aerosol loading for both weather and climate applications, and searching for biological hazards. Many of these investigations include comparisons of measured scattering characteristics with those of model particles whose ELS properties are determined computationally. While computational capacity continues to increase, calculating the scattering pattern or Mueller matrix accurately for an arbitrarily shaped particle remains challenging. To reduce this computational burden, approximations are frequently employed, which can take various forms. One approach is simplifying the particle shape to a geometry for which it is easy to obtain an exact solution (e.g., a sphere or spheroid). Another is to use approximate models that are valid when the particles are either much smaller or much larger than the wavelength of the incident light (Rayleigh scattering and geometric optics, respectively). Here we briefly outline the main theoretical methods for computing ELS properties.

2.1. Small-particle approximations

One of the simplest ELS solutions can be achieved under the assumption that the size of the particle is much smaller than the

incident wavelength and the complex refractive index is not large. In this case, the problem can be treated using electrostatic theory. Within this Rayleigh approximation, the ELS intensity is proportional to V^2/λ^4, where V is the volume of the particle. A common misconception is that the ELS phase function of particles in this small-particle limit is independent of particle morphology, a strict derivation reveals this function depends on the strength of the individual dipoles induced within the particle system [21]. Regardless, it is difficult to retrieve characterizing information from biological particles within this size regime.

2.2. Soft-particle approximations

There are several manifestations of the soft-particle approximation, also referred to as the Rayleigh-Gans-Debye approximation [40,52,154], Born approximation or anomalous diffraction approximation (ADA). The central premise is that the refractive index of the particle is small $|n - 1| \ll 1$, so that an incident plane wave passes through the particle unperturbed. The scattered field can be retrieved through an integration over the induced dipole moments within the particle volume. Additionally, some versions of the approximation require limitations on the size: $x|n - 1| \ll 1$, where the size parameter $x = 2\pi a/\lambda$, and a is the radius of a volume-equivalent sphere. It is possible to obtain analytical expressions for various simple, non-spherical shapes such as disks, needles, or a continuous distribution of ellipsoids, which, for example, have been compared with measurements of the clay component of mineral dust aerosols [73]. These approximations are all simple to implement in a few lines of code and can even be extracted from the discrete dipole approximation (DDA) codes by not including dipole-dipole interactions. They are especially useful for biological samples in solutions, in which the differences in refractive index between the particle and solution is small [97]. For airborne aerosol particles, the approximations have limited usage because of the much larger differences in refractive index between the particle and air medium [36].

2.3. Spherical particles

Lorenz-Mie theory is the solution to Maxwell's equations for the scattering of an electromagnetic wave incident on a homogeneous sphere. Reviews and derivations can be found in references (e.g., [21,176]). There are several publicly available codes for the calculation of Lorenz-Mie scattering efficiencies and phase functions as in Fortran [21], Matlab [105], Python [151], C (Prahl & Jaques), and Julia [190], as well as codes that extend to multi-layered spheres. The Lorenz-Mie solution is useful when the size of the scattering particles is similar to the wavelength ($x \sim 1$). The obvious limitation is that not all particles are well-approximated by a sphere, however this is sufficient for certain types of aerosols such as cloud droplets.

2.4. Geometrical optics approximation

When particles are large in size, there are limited methods that can be used to calculate their ELS. The geometrical optics approximation, also called ray tracing, is a Monte Carlo technique in which the incident field is described by rays that are incident upon the particle at different locations. At each interface, the rays are either transmitted or reflected until they reach the far field, another interface, or are absorbed by the medium. For this approach to be valid, the size of the local surface components and their local radius of curvature must be much larger than the wavelength of the incident light. The most familiar application for geometrical optics is studying the refraction and reflection of light by lenses and mirrors. It can also be used to describe atmospheric constituents such as large cloud droplets or ice crystals [101]. In this ray-tracing method, wave effects like diffraction are not included, but can be incorporated separately.

2.5. T-matrix methods

T-matrix methods can be used to calculate the ELS from irregularly shaped particles, whose boundary can be expressed as a function of (θ, φ). The method relies on separation of variables and each component of the electromagnetic field is expanded in a series of vector spherical harmonics. The transition matrix, or T-matrix, relates each harmonic of the scattered field to each component of the incident field. It is especially useful because rotation can be operated on the T-matrix to address different particle orientations and analytical expressions exist to perform orientation averaging. Lorenz-Mie theory is a special case of a diagonal T-matrix. The T-matrix can be calculated directly from the particle shape, size parameter, refractive index, and orientation [115,188]. The T-matrix method has been used extensively to calculate the orientation-averaged light scattering from spheroids. These model simulations have been used to retrieve the optical properties of aerosols, including desert dust (e.g., [47]).

The greatest challenge in using T-matrix theories is calculating the actual T-matrix. One of the most commonly used methods is the extended boundary condition method (EBCM) because it is greatly simplified for bodies with rotational symmetry (e.g., [114]), although there has been a limited amount of work on other shapes including triaxial ellipsoids, as outlined in a list given by Mishchenko [113]. One additional feature is that T-matrices of different particles can be combined to produce a T-matrix of an aggregate system (e.g. [102]. For these cases, T-matrix calculations are fast compared to other numerical methods for calculating optical properties of particles having non-spherical morphology. Another method of calculating the T-matrix is the point matching method (PMM). In the PMM, the boundary conditions of incident, internal, and scattered fields are matched at points on the particle surface [122]. One issue with calculating the T-matrix is inaccuracies when the particles are large or have large eccentricities. One recent method to calculate the shape matrix resulted from the discovery that shape dependence could be separated from the size and refractive-index dependence of the T-matrix. The shape matrix, or Sh-matrix, contains only information about the particle morphology [140]. For many systems, like spheroids, Chebyshev particles, and even arbitrarily shaped particles expressed as a function of (θ, φ), this shape matrix can be calculated analytically [145]. The size and refractive index can be incorporated into the Sh-matrix to form the T-matrix using analytical operations; thus, a completely analytical method for calculating the T-matrix, and ELS properties from irregularly shaped particles exists. In addition to not suffering the issues with inaccuracies of other methods [144], a further advantage of this method is that because the size and refractive index are incorporated after the Sh-matrix is calculated, particle polydispersions and spectral studies can be performed at reduced computational costs. The shape matrix has been used to find the T-matrix analytically from complex models resembling spores [141] or even the coronavirus [147].

2.6. Finite-difference time domain (FDTD) methods

Like the DDA, discussed below, the FDTD method uses a discretization scheme to maximize utility. Unlike all the other systems discussed here, the solution is achieved in the time domain, but tracing a pulse through the discretized system using a finite-difference method and a differential form of the Maxwell equations [197]. In Yee's method, the E- and H-fields are shifted by a half-step in both the space and time domains, then the equations are

solved in a leapfrog manner, where first the E-field values are calculated, then the H-field values, and so on until the system reaches a steady-state or the transient behavior is evolved.

One major source of errors has been spurious reflections from the edge of the grid, which have been removed using novel applications of absorbing boundary conditions [173]. Because of their widespread use in other fields, these methods were parallelized relatively early and have been applied to the study of aerosols and creation of ELS databases for radiative transfer applications [196]. Due to the fact that the grid spacing must be small compared to wavelength, while at the same time the simulation space must be large enough to encompass the particle, the FDTD may require a large number of computation points, limiting its usage for large particles.

2.7. Discrete dipole approximation (DDA)

In the DDA method, shapes are constructed within a 3D grid whose lattice points are treated as polarizable dipoles. This array of polarizable points can accurately approximate the response of a continuum target on length scales that are large compared with the inter-dipole separation. This idea was developed to investigate dust aggregates in the astrophysical environment [153]. Various codes are publicly available, contributing to the method's widespread use, including DDSCST [46] and ADDA [198]. The advantage of this method is that the discretized system can represent a completely arbitrary, heterogeneous particle. However, the computation time increases with the number of dipoles and can be extremely computationally intensive, as to be impractical for large particles. The DDA method has been used, for instance, to investigate the absorption efficiency of black carbon produced via biomass burning [106].

While there are several models that can be used to calculate the ELS patterns or Mueller matrix of particles in various shapes, each come with accompanying restrictions. Many of these can be used to create an inverse model or lookup table to retrieve size distributions and, with the exception of Lorenz-Mie theory, shape information from field or laboratory measurements. In addition to the various codes referenced above, there is a useful repository of publicly available scattering codes [163].

3. Advances in experimental technologies and instrumentation

Aerosol is a diverse mix of complex particles. For an apparatus or instrument to be able to obtain the individual particle properties among a large number of mixed aerosol particles, e.g. bioaerosol particles within atmospheric aerosol particles, single-particle measurements are required. However, measuring the ELS from individual micrometer-sized particles is a challenging endeavor. In this section, we outline the amazing advances that have occurred over the last century [82,88].

3.1. Detecting light scattering at a single fixed angle

After Ludvig Lorenz and Gustav Mie developed the theory of ELS for spherical particles [99,109], experimentalists attempted to verify the theoretical predictions, and afterward used the 2D and 3D solutions to verify their instrumentation (e.g., [13,22]). The dilute solutions (i.e. colloidal suspensions) in which multiple scattering by inhomogeneous particle populations could make results difficult to interpret. It was at this time that scientists started to perform the ELS experiments on *individual* particles of smoke. Using a Ramsden eyepiece, they viewed falling individual smoke particles by capturing scattered light at a polar angle of 90° [137]. The rate of falling provided insight into the size of the particle, while the brightness of the particle was used as a measurement of scattering

intensity. It should be noted that this setup was similar in design to the one used by Millikan and Fletcher to measure the charge to mass ratio of an electron [111].

The next advance was the creation of an optical particle sizer. This effort was realized by Gucker et al. [61], who measured the flash intensities of scattered light generated from a fine stream of aerosol particles traversing through an intense light beam. The flash intensities were roughly correlated with the sizes of the particles. Gucker et al. were able to measure the scattered light at multiple angles. Fig. 2 shows the development of various optical schematics for collecting scattered light from single aerosol particles, it is advanced from (a) to (f), corresponding to the description in Sections 3.1-3.5.

3.2. Detecting light scattering at multiple angles in a single scattering plane

In 1961, a device was constructed to detect multi-angle ELS in a single scattering plane that covered the polar angle from 40° to 110° with a resolution of 5.2° using a photomultiplier tube (PMT) on a motor-driven rotation stage from a particle that was electro-dynamically levitated [60]. A decade later, an instrument called the Differential II was developed to detect scattered light using solid-state electronics over a larger polar-angle range from 10° to 170° with a 2° angular resolution (Phillips et al., 1970). This device could extract some information about morphology and refractive index from homogenous spheres, coated spheres, and bacterial spores [192].

The particle levitation requirement greatly restricted the throughput capabilities in measurement. The next step in the maturation of the instrumentation was accomplished with an extremely clever design involving an ellipsoidal reflector, a rotating disk with a pinhole, and a single PMT. The new instrument was able to measure angularly resolved ELS from individual aerosols in a laminar flow [62]. This design was further improved using a photodiode array, rather than a single detector, which approached a data-collection rate of 1000 particles/sec [12].

3.3. Detecting light scattering from a range of azimuthal angles

The instruments discussed so far collect light scattered at a fixed azimuthal angle. While the scattered light from a symmetric system, like a homogeneous sphere illuminated by circularly polarized light, will not have an azimuthal dependence. Once this symmetry is broken, there will be an azimuthal dependence to the scattered light. Measuring the azimuthal dependence thus provides a means of characterizing particle asymmetries, and instruments were designed to detect light at multiple azimuthal angles at a fixed polar angle in an attempt to classify aerosol particles by shape. Paul Kaye and collaborators developed a series of instruments incorporating fast-response PMTs with dedicated electronics for data acquisition and classification algorithms, which could detect and analyze up to 50,000 particles over a 5-second data collection window [83,85,160]. Advanced designs utilized different numbers of PMTs at different polar angles which could rapidly classify particles based on symmetries.

3.4. Detecting light scattering at multiple polar and azimuthal scattering angles

The DAWN-A instrument was developed to measure the ELS at various azimuthal and polar scattering angles from particles in a flowing gas stream. In particular, an aluminum spherical chamber was designed with 72 ports. The ports were arranged on four great circles with 18 ports on each circle, representing four different azimuthal angles. This design allowed a user to measure ELS at var-
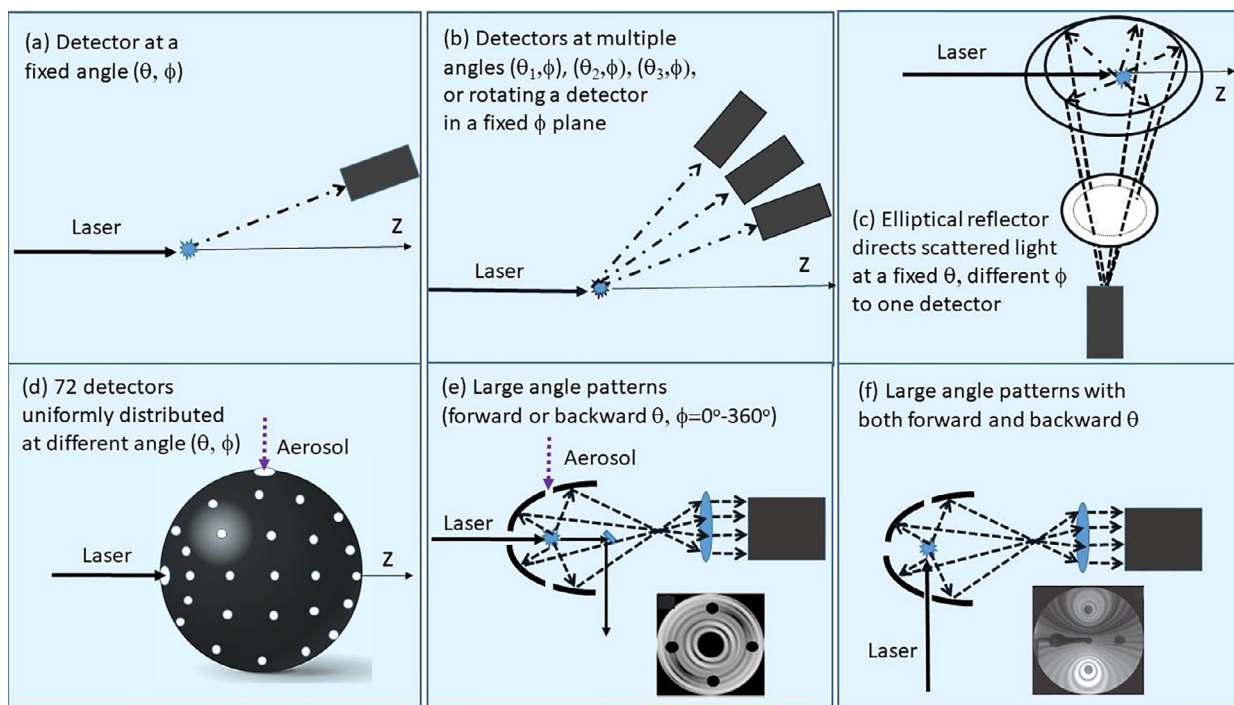
Fig. 2. The development of various optical schematics for collecting scattered light from single or multiple aerosol particles.

ious polar scattering angles at a fixed azimuthal angle or various azimuthal angles at a fixed polar scattering angle. Fiber bundles coupled to photodiodes were used to capture the scattered light from a particular port and measure their intensities [193].

3.5. Detecting angle-resolved light-scattering patterns

The emergence of 2-dimensional charge-coupled device (CCD) provided a pathway to detect angularly resolved ELS patterns. In particular, incorporating an intensified CCD into the detection plane with an ellipsoidal reflector was able to collect 84% of the solid angle of scattered light, the captured ELS patterns supplied a detailed image of the angular dependence of the ELS [83,86]. The apparatus detected scattered light over a polar-angle range 30° to 141° and azimuthal-angle range 0° to 360° with a 385 × 288 pixel detector.

The distortions due to aberrations associated with the large collection angle of the ellipsoidal reflector, prevented the ELS patterns from being quantitatively compared with theory precisely. The design was simplified, so that only the forward scattering pattern was detected within a cone of ~30° with a high f-number lens to reduce the misalignment effects. In addition, using a photodiode array chip to replace the ICCD detector, similar to Bartholdi's design, dramatically increased the detection rate of particles [81].

Lenses as collection optics have been used to capture far-field ELS patterns from spherical and nonspherical particles in the 1970s and 1980s [7]. In the late 1990s, Richard Chang's group at Yale University captured high-angular resolution ELS patterns from aerosol clusters using an $f/1.2$ camera lens labeled as TAOS (Two-dimensional angular optical scattering) patterns [69].

In the 2000s, Pan et al. [129] incorporated an ellipsoidal reflector and a 1024 × 1024 pixel ICCD in the apparatus, similar to that of Kaye et al. [81], and increased the detection of scattered light to over 2π steradians in high angle resolution. This was further developed to capture patterns that contained scattering light in both the near-forward and near-backward directions [5,50]. Aberrations, particularly for slightly misaligned particles, could dramatically re-

duce the quality of the captured ELS patterns. The solution to this issue was an ingenious cross-beam trigger system which only illuminated aerosol particles when located in a well-defined scattering volume, which is in the depth field of the reflector [5,134]. In the 2000s and 2010s, scientists also began exploring multiple-laser illumination to capture simultaneously the scattering patterns at different wavelengths [3,70,93]. Furthermore, by utilizing optical trapping to levitate a single particle, Pan et al. [135] was able to measure ELS in the backward hemisphere, extended to the exact backward angle ($\theta = 167.7°$ to 180°, $\phi = 0°$ to 360°).

3.6. Polarimetry

The greatest advance in experimental light scattering is undoubtedly the polarization modulation technique of Hunt & Huffman [75,76]. This technique allows for the rapid, accurate measurement of the entire light-scattering Mueller matrix and despite numerous advances in optical apparatii, has remained unchanged in half a century. The technique employs an optical modulator that cycles through the polarization states at typically 50 kHz. This greatly reduces experimental error, since any change in the sample during the measurement of the different polarization states will lead to experimental error. This development actually makes it possible to measure accurately the polarized light scattering from a levitated particle or even living cells. After Hunt and Huffman's original device, a number of other similar devices were constructed using the same technology. Equipped with a rotating goniometer to cover a scattering-angle range from nearly 0° to 180°, a laser, electro-optic modulator on the incident beam and a polarizer, ¼-wave plates and a photomultiplier tube (PMT) on the receiving end, these devices could measure the Mueller matrix one element at a time (e.g. [31,107,116]; Schnaiter et al., 2012). The method has been employed to verify the theory of light scattering from an infinite cylinder [13] and a single sphere [22]. The technique was first recognized as a potential biophysical tool by Bickel et al. [16] and subsequently has been used to characterize cells [17], bacteria [23,24,177,178], pollen [31,54], phytoplankton [183] and even
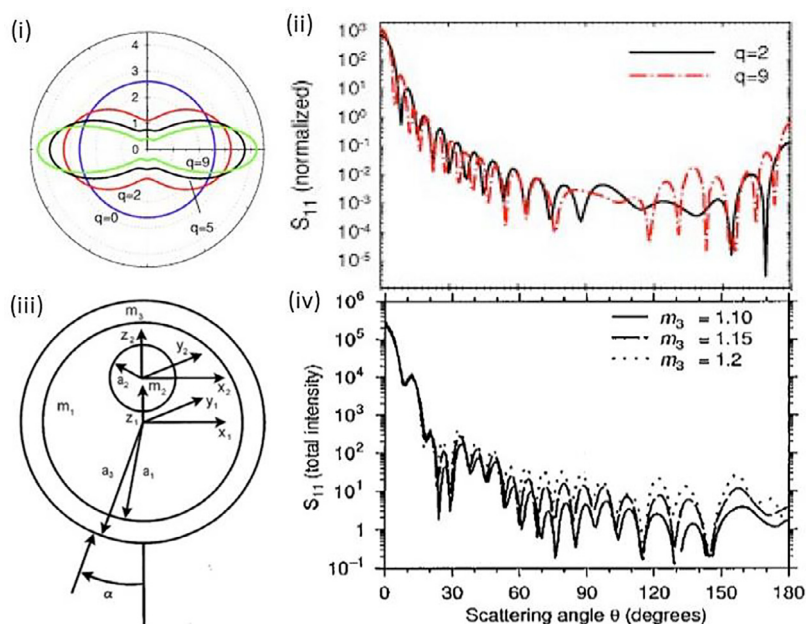
Fig. 3. (i) Geometry of a simulated blood cell having different biconcave disk shapes and (ii) its corresponding calculated ELS phase function $I(\theta)$ with different deformation degrees $q = 2$ and $q = 9$. Reprinted from [100], with permission under open access Creative Common CC BY license; (iii) Geometry of a simulated spherical cell and (iv) its phase function $I(\theta)$ having three different cell membrane refractive indices $m_3 = 1.1$, 1.15, or 1.2. Reprinted from Videen & Ngo [180], with permission under open access Creative Common CC BY license.

muscle fibers [53]. We note that because of the nature of the go-niometer, which would require that a single particle remain steady during measurement, most work using the such devices has been on multiple particles in a cloud or solution and technically beyond the scope of this review; however, the results suggest that such polarimetric techniques could be valuable in future studies.

Finally, we note that the Granada-Amsterdam light-scattering database is a tremendous resource (https://www.iaa.csic.es/scattering/index.html), providing the largest collection of experimental light-scattering Mueller matrix elements of aerosol particles. The device has undergone many improvements in its over two decades of data collection, providing light-scattering data from numerous samples collected at multiple wavelengths [117]. Data have been collected from multiple mineral samples, like clays and Saharan dust, that may interfere with the detection of bioaerosols [117–119]. The apparatus measures the light scattering from polydispersions of particles passing through the beam, so these are not single-particle measurements; however, they do provide a reference frame of what average light-scattering Mueller-matrix elements look like for various sample types. One primary function of the database is the validation of light-scattering models, so it is necessary to integrate the light-scattering results over the size distribution, as well as to take into consideration the random orientation of the particles [48,182,201,202].

4. Retrieved information from ELS measurements

As discussed above, we should be able to calculate the ELS patterns $P(\theta, \phi)$ from virtually any kind of single particles whose size is comparable to the wavelength of the incident light, and any fine change of the scattering particle should be reflected in the ELS pattern. These changes can be the overall size and shape, particle chemistry that is contained in the complex refractive index, and particle orientation and position related to the illuminating light. Fig. 3 gives an example of how the scattering phase function $I(\theta)$ from a single cell can change with different deformed degrees of shape [Fig. 3(ii)], or varied refractive indices of the cell membranes [Fig. 3(iv)]. They are calculated using the FDTD method based on

a biconcave disk shape for a red blood cell (RBC) [100], and the T-matrix method of an ideally spherical shape with different refractive indices from nucleus, cytoplasm, and membrane [180], respectively. The calculations show large variations of $I(\theta)$, even with only a small change of one parameter. The intensity from the two calculations show a large difference as the geometrical shapes of the cell model are quite different as shown in Fig. 3(i) and (iii), although the two enveloping curves of the scattering peaks have some similarity. The results presented in Fig. 3 showed how complicated the scattering phase function could be, not to mention the scattering patterns under different parameters, shapes and refractive index, of a real cell.

Fig. 4 showed ELS measurements of intensity $I(\theta)$ from individual single RBCs at different controlled orientations during stretching using a double-beam tweezers (left), which are in good agreement with theoretical simulations [90]; Another example from the angularly resolved ELS patterns measured from individual single *B. subtilis* spores also showed good agreement with the simulations at different related orientations and polarizations of the incident laser beam as indicated in (a), (b), (c), and (d), respectively (right, [9]). These calculations reproduced the experimental observations with relatively precise detailed structures of the patterns. In another words, the advanced computational ability is able to calculate the ELS patterns from a well-defined particle (shape, size, refractive index etc.) to replicate the experimental observations. However, it is still a big challenge to retrieve the properties or parameters of the scattering particle from its scattering patterns, i.e., the reverse process. In the sections below, we will review what we can get from the measurements, particularly on how we can use ELS to detect and characterize bioaerosol particles.

4.1. Size and refractive index

Numerous instruments have been developed to size particles based on their ELS measurements. These can be based on ELS measurements obtained as individual particles pass through a beam or from a suspension of many particles, most often in solution. Typically, they can measure particle sizes ranging from 10 nanome-
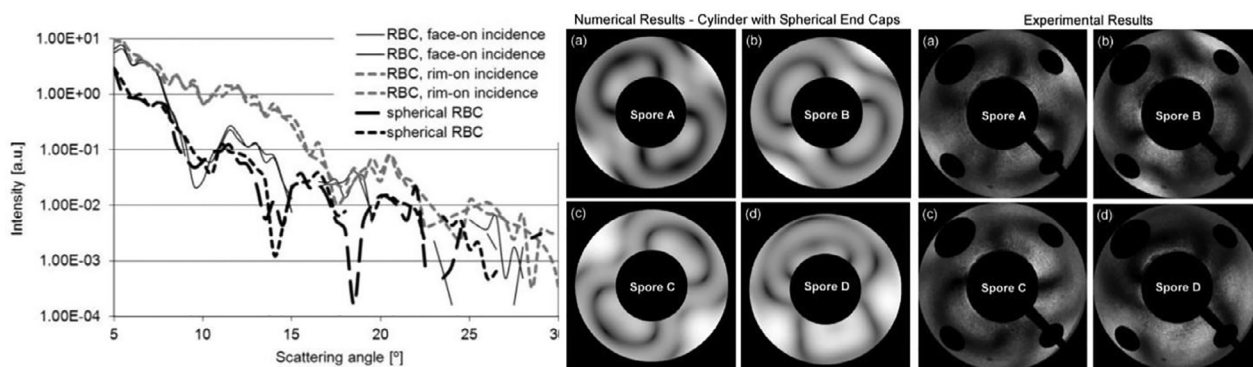
Fig. 4. Left: Measurement of near forward $I(\theta)$ from individual RBC with different shapes and orientations illuminated by a 632.8 nm He-Ne laser polarized at 22° from the vertical position [89]. Reprinted with permission of The Optical Society. Right: comparison of calculated and experimental ELS patterns from single *B. Subtilis* spores with different orientations and polarizations of the incident laser beam [9]. Reprinted with permission of The Optical Society.

ter to a few tens of micrometer using a single photoelectronic detector or multiple detectors as described in Section 3. These instruments include the laser aerosol spectrometer or optical particle sizer from TSI, multi-angle light scattering (MALS) detectors for nano-size particles from Wyatt Technology, particle size analyzers from Anton Paar, or particle size analyzers from ATA Scientific Instruments. These instruments generally are calibrated using measurements of NIST traceable Polystyrene Latex (PSL) microspheres, and the scattering particle size obtained are those of a PSL microsphere that has the most similar scattering response as the measured particles. If the particle is closer in shape to a spherical particle with a refractive index similar to that of PSL, the measured particle size could be more accurate. One issue with such instruments is that the response functions may not be monotonic, potentially leading to erroneous results even if the particles being measured are spherical with the refractive index of PSL [68].

4.1.1. Spherical particles

While very few classes of particles resemble homogeneous spheres, we discuss them in this section because so many studies use Lorenz-Mie theory to simulate the ELS. The reason for this primarily is the convenience of having the codes widely available and the rapidity with which such calculations can be made. Because of their symmetry, the ELS from spheres is characterized by very strong angular resonances, which makes their scattering significantly different from all other particles. As such, unless the particles under study are nearly spherical in shape, the usage of Lorenz-Mie theory to simulate their ELS is likely a poor choice. We illustrate the strong angular resonance structure in sample calculations shown in Fig. 5, produced using the free MiePlot program provided by [94]. A few general conclusions about ELS from a sphere can be summarized as follows:

1. The ELS patterns formed by spheres illuminated by unpolarized or circularly polarized light appear as concentric circles, which oscillate along θ. Their frequency increases as sphere size increases, providing a simple means of sizing. As shown in Fig. 5, if a detector is placed at a specific angle θ, the light intensity oscillates with the increasing particle size, and there is no scattering angle θ where a simple monotonic intensity change occurs with increasing particle diameter, making sizing using a single detector a problem plagued by non-uniqueness. The structure of the oscillations depends on scattering angle. Light scattered at small scattering angles in the very near-forward direction is dominated by diffraction; whereas, at larger angles reflection and refraction, and interference effects play a greater role. These effects have a greater dependence on refractive index and absorption. In general, multiple detectors with multiple
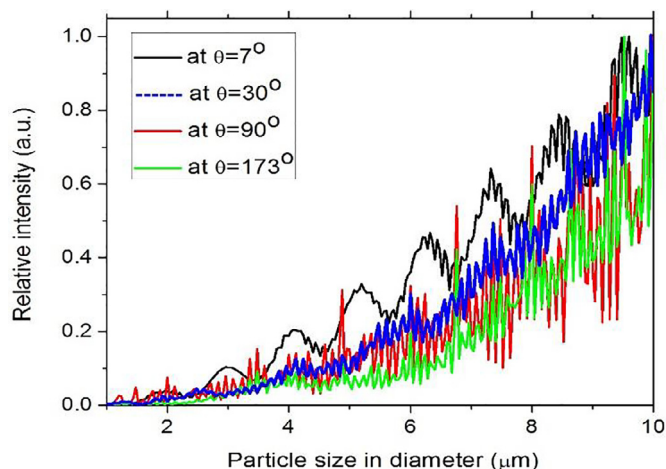

Fig. 5. ELS intensity varies with particle size ($n = 1.5$, absorption $= 1.82 \times 10^{-9}$) illuminated by a vertically polarized Gaussian beam (532 nm, waist diameter $= 40$ μm) at different detection positions ($\theta=7, 30, 90, 173\pm5°$ and $\phi=90\pm5°$). The maximum intensities of all curves are normalized to 1 for easy comparison.

illumination wavelengths are necessary to obtain more accurate size determination [1,152].

2. With a detector placed at a set scattering angle θ, the intensity generally follows an oscillating curve as the real part of refractive index changes and follows an exponentially decaying curve as the imaginary part of refractive index (absorption) increases. Therefore, it is more challenging to retrieve the particle size accurately when the particles have absorption different from the PSL spheres used for calibration [3,63,77,184].

3. Particle size can be determined accurately using optical whispering-gallery modes (WGMs), also known as morphology dependent resonances (MDRs). Spheres are excellent resonators and when resonance conditions are met, their extinction can increase dramatically [6,8,32–35,179]. The periodicity of the resonances depends strongly on size and refractive index, so it is possible to characterize these properties by measuring the distances between resonances as size parameter x is varied. This can be done by illuminating the sphere with a broadband source or by monitoring the intensity as a liquid sphere evaporates [65,80,120]. Another method is to examine the WGM resonance peaks in Raman or fluorescence spectra [1,11,65,80,91,125,152].
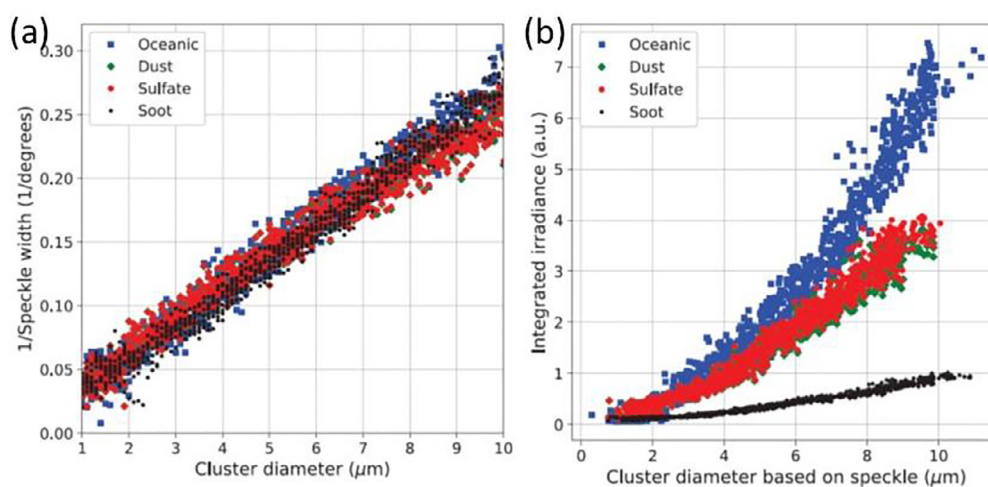
Fig. 6. (a) Linear correlation between the diameter of aggregates and the average speckle width, regardless of particle composition; (b) Integrated scattering intensities change with cluster diameter, indicating different absorptions of aggregates. Reprinted from Walters et al. [184], with permission of Elsevier (www.elsevier.com).

4.1.2. Non-spherical, irregular-shape particle

For several reasons, characterizing non-spherical particles is even more difficult than spherical particles. The scattering intensity distribution from a non-spherical particle does not form symmetric rings, but depends on both the polar angle θ and the azimuthal angle φ, in addition to the orientation of the particle. The latter dependence can hamper retrievals based on diffraction. For example, if the particle is non-spherical the positions of the interference minima will depend on the orientation. If the sizing is of a population of particles, in solution for example, scattering structure will smooth, making it difficult or impossible to size using minima positions, as these may not even exist.

One method that has been used successfully is to examine the separations of the speckles/islands that appear in the single-particle ELS patterns. This speckle has a strong linear correlation with the overall size of the scattering particle. For instance, Holler et al. [71] showed there is a correlation between the mean number of the peaks and valleys in the scattering patterns and the diameter of aggregates formed of micro-spheres. Similarly, it was reported that the median surface area of intensity peaks is inversely proportional to particle size with particles having rough surfaces and complex structure, including mineral dust, spores, pollen, ice analogs and sphere clusters from 4 to 88 μm in size. The averaged speckle size can be expressed as

$$Ds \approx 4\lambda z/\pi D \qquad (4)$$

where z is the distance between the particle and the detection plane, and D is the diameter of the uniformly illuminated area, equivalent to the 2-D size of the scattering particles [175]; Another finding is that the dimensions of a particle can be obtained by analyzing the central peak of the 2D-autocorrelation of the speckle pattern [25], and the overall size of an irregularly shaped particle (2-10 μm in diameter) is inversely proportional to the nominal width of the speckle ($\Delta\theta$) [184], or

$$\Delta\theta = 37/D \qquad (5)$$

where D is the equivalent diameter of the cluster. This formula works regardless of particle absorption. In addition, Walters et al. [184] found that the integrated scattering intensity is inversely correlated with the imaginary part of the refractive index of the constituent spheres in the cluster (Fig. 6(b)). Based on these studies, the overall size of an irregularly shaped particle can be obtained from the average size, number, or nominal width of the speckles,

and then, the absorption can be retrieved from the integrated scattering intensity.

ELS has been used to characterize particle size in bioaerosol detection, which has been used to normalize the fluorescence intensity to obtain the quantum efficiency or the cross section of fluorescent aerosols [87,128,131–133,156]. It was also able to characterize shape by comparing the asymmetrical factor (*Af*) with those of bioaerosol particles [4,84,157,162]. Using the combined signatures from the illuminations of two laser wavelengths (261-nm and 351-nm), the excited fluorescence spectra and the ELS intensities have been used to discriminate target bioaerosol particles, like *B. subtilis spores,* against natural atmospheric aerosols over 25 h of continuous measurements from ambient air [132]. Such measurements can also supply information for distinguishing different pollens and fungal particles [131]. Bioaerosols, including aggregates formed of virus or bacteria with sizes ranging from a few tens of nanometers to a few microns, have real parts of refractive index of $n_r \sim 1.2$–1.6 with the imaginary part ranging from $n_i = 0.00$ to 0.30 [59,191]. The overall shapes of the aggregates appear spherical in shape with rough surfaces as revealed by the SEM images [2,71,129]. For atmospheric aerosols, the real part of the average refractive index was found to be between 1.52 and 1.57, the average imaginary part varied between 0.031 and 0.057 from the analysis of 15,500 particles in the size range of 0.1 to 25 μm. These particles were classified into 10 different groups: ammonium sulfates, calcium sulfates, sea salt, metal oxides/hydroxides, carbonates, silicates, soot, biological particles, carbon/sulfate mixed particles, and rest of carbon-rich particles [49]. Note that all n_r and n_i values are dependent on the illumination wavelength.

4.2. Q-space analysis and power-law

The diffraction process can be viewed as a Fourier-transform operation that maps a system's spatial frequencies. To utilize this process, *Q*-space analyses consider the intensity as a function of the scattering wave vector $q = \left(\frac{4\pi}{\lambda}\right)\sin\left(\frac{\theta}{2}\right)$ on a log-log plot. The intensity in Q-space corresponds to the magnitude of the spatial frequencies q in the scattering system. *Q*-space methods are used for analyzing surfaces with the bidirectional reflectance distribution function (BRDF) [121], sizes of particles in solutions in dynamic ELS applications, and also to size and characterize single particles [15]. In the latter application, the scattering intensity can be described in terms of power laws with quantifiable exponents
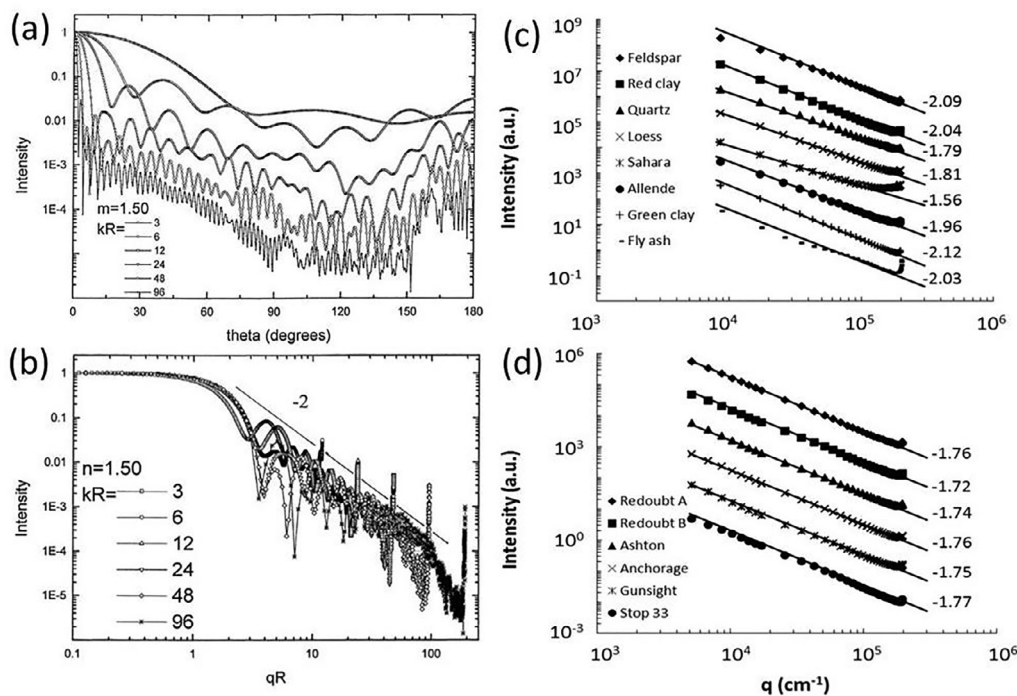
Fig. 7. (a) Normalized Lorenz-Mie scattering phase functions $I(\theta)$ for $n_r = 1.5$ spheres of different size parameters kR; (b) same as (a) but plotted logarithmically versus qR with a line having slope of -2 from Sorensen [170], printed with permission from Elsevier (www.elsevier.com). (c) and (d) Q-space plots of phase functions $I(\theta)$ as a function of q with 15 different aerosol particles, reprinted from Sorensen et al. [171] with permission under open access Creative Common CC BY license.

[170]. Fig. 7(a) shows an example of Lorenz-Mie scattering phase functions from $n_r = 1.5$ spheres of different sizes expressed in size parameter kR. The dominant features are the angular resonances inherent for highly symmetric spheres. Fig. 7(b) shows the same data plotted as a function of dimensionless parameter qR. These plots appear to be related in a more coherent manner. Although the angular resonances still exist, a power law can be used to describe the envelopes of the plots at large qR [170]. For a sphere of arbitrary size and real refractive index, the scattering phase function can be divided into five major regimes in Q-space: (1) the forward scattering lobe (the Rayleigh regime with $qR < 1$); (2) the Guinier regime ($qR \approx 1$); (3) the power-law regime at large qR; (4) the hump; and (5) the glory regime [170,171]. Envelopes of intensities in some regions can be characterized by the following:

$I \approx (qR)^0$, when $qR < 1$,

$I \approx (qR)^{-2}$, for the tangent line connecting the Guinier bend to the hump,

$I \approx (qR)^{-3}$, in the region preceding the hump,   (6)

$I \approx (qR)^{-4}$, in the region following the Guinier bend for the Rayleigh-Gans-Debye limit: $\rho' < 1$, where $\rho' = 2kR\left|\frac{n^2-1}{n^2+2}\right|$ is the phase-shift parameter. The Q-space analysis provides a rapid means of sizing a sphere by finding the intersection of the lines enveloping the first two regions.

Q-space analysis has been applied to a number of particles other than spheres, including soot fractal aggregates [172], and many irregularly shaped particles such as dust [187], ice crystals, clay, ash and over 50 different samples [66,162]. Spheres are great resonators and their Q-space plots have features that are not apparent in those for irregularly shaped particles. For instance, irregularly shaped particles do not have a hump and typically only display one form of power-law decay. While the power-law index for spheres appears to take on integer values, this exponent can take on non-integer values for irregularly shaped particles and is different, depending on the sample. Fig. 7(c) and (d) show Q-space

curves measured from different samples. These curves have much less structure than those of spheres. It is much easier to obtain a power-law index from these curves than for spheres, as they can fit a line to the linear portion of the curve, rather than enveloping the curve. Also obvious in these curves is the intensity surge that occurs at large values of q. In these curves the forward-scattering lobe are not shown. In this case the particles are too large for the detector system to measure this lobe, making it impossible to measure the particle size from these particular samples. These studies show that this simple and comprehensive description of scattering in terms of quantifiable power laws can be used to differentiate scattering by particles of different shape [66,171]. Q-space analysis provides a different perspective in describing and understanding ELS. It reveals power-law functionalities of the wave vector q providing means for analyzing length-scale dependencies. It systematically describes the magnitude of the scattering and the interference ripple structure. We expect such Q-space analyses will also be applied in bioaerosol discrimination against other aerosol particles.

4.3. Degree of symmetry in particle shape

Any irregularity in particle morphology will result in an asymmetrical scattering intensity distribution around the azimuthal angle ϕ. At small scattering angles, the ELS is dominated by diffraction, which has a Fourier-transform relationship with the particle [82,86]. The asymmetrical factor (Af) was introduced to characterize the shape of a particle from the diffraction component. Many bioaerosols, especially bacterial spores and cells, have shapes similar to capsules, i.e., a finite cylinder covered by two hemispheres at its ends. The diameter of the cylindrical portion is typically around 0.5–1 μm, and the length varies from 1–4 μm depending on the growth media and preparation conditions [9,67,78]. Viruses are much smaller, having dimensions from a few 10 s of nm (e.g. adeno-associated viruses and MS2) to a few hundred
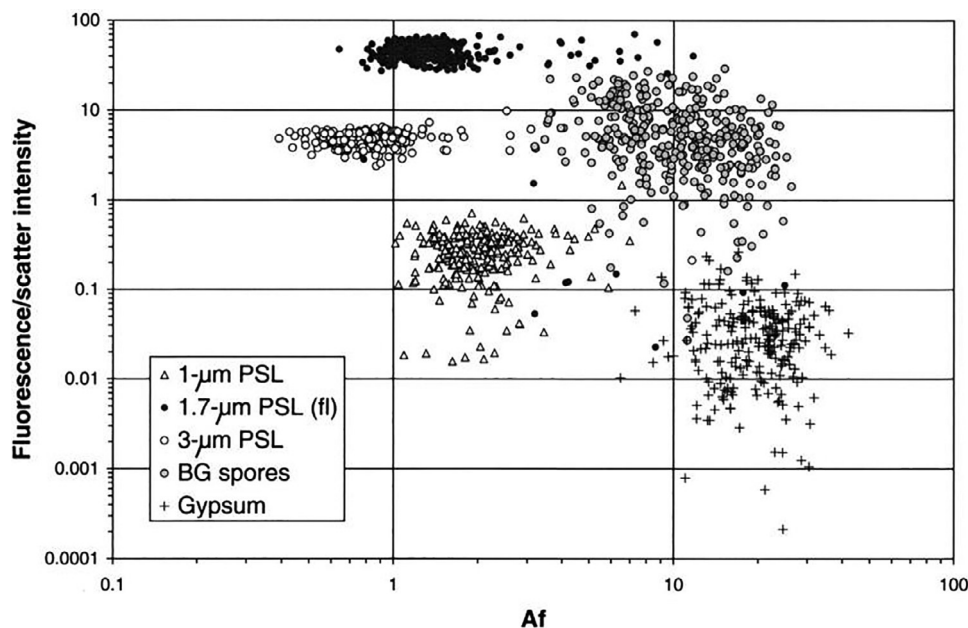
Fig. 8. Scatter plot of the fluorescence amplitude normalized to the elastic scattering intensity as a function of *Af* for PSL spheres, gypsum particles, and *B. subtilis* var. niger (*BG*) spores. Reprinted from Kaye et al. [84], with permission of the Optical Society.

nanometers (e.g. coronaviruses and poxviruses). These commonalities in dimensions result in specific *Af*s for each different kind of bioaerosol particles, which can help to differentiate them. Initially, the *Af* was used to separate spherical from non-spherical particles, but it was found useful in discriminating between different types of non-spherical particles as well [5,82–84,86,157,162].

Fig. 8 shows how *Af* provides an effective means of particle discrimination among different sizes of florescent and non-fluorescent PSLs, gypsum particles, and the *B. subtilis* var. niger (*BG*) spores associated with fluorescence and scattering intensity [84]. Here, the *Af* is defined as,

$$Af = C\left[\sum_{i=1}^{n}\left(\bar{E} - E_i\right)^2\right]^{1/2} / \bar{E} \qquad (7)$$

where *n* is the number of pixels in a ring along ϕ of constant θ, *E* is the measured scattering intensity from each pixel from a specially designed circular sensor, $\bar{E}$ is the average intensity of all *E*, and *C* is a normalizing constant to render the maximum possible value of *Af* to be 100. Ideally, spherical particles should generate equal scattering intensity at each pixel in the azimuthal ring and produce an *Af* = 0. In other cases, a parameter named sphericity index (*SPX*) was introduced to describe the measured aerosol particles [43,161]. For a spherical particle, the value of *SPX* was designed to be 1. Another similar parameter to *SPX* is the degree of symmetry (D_{sym}), expressed as

$$D_{sym} = 1 - \sum_{pixel\ subset}\left|\frac{I^N(\theta, \phi) - I^N(\theta, \phi + 180^o)}{2}\right| \qquad (8)$$

where $I^N(\theta, \varphi)$ is the normalized single pixel intensity at (θ, ϕ). For a spherical particle, the two pixels at (θ, ϕ) and $(\theta, \phi + 180^o)$ should have the same scattering intensity, and the D_{sym} should be equal to 1 as *SPX*. In addition, if the aerosol has an axis of rotational symmetry that is pointed either parallel or perpendicular to the incident polarization, the scattering pattern will also have 180° rotational symmetry, again resulting in a D_{sym} value of 1 [2,5].

Fig. 9 shows how D_{sym} depends on particle shape over a wide range of scattering intensities indicated by the mean number of photoelectron counts (proportional to scattering intensity) per pixel on the abscissa. These values of D_{sym} and scattering intensities were calculated from the ELS patterns recorded in the backward scattering hemisphere from PSL spheres (39 patterns), droplets of dioctyl phthalate (200), particulate matter in diesel exhaust (288), single or small clusters of *B. subtilis* spores (97), and ambient aerosol particles (5993). It is not a surprise to learn that both the PSL spheres and dioctyl phthalate droplets have the highest D_{sym} (>0.75) as they are expected to be nearly spherical. The majority of the particulate matter in diesel exhaust have D_{sym} values above 0.70 with a maximum of 0.85. This suggests that the diesel exhaust formed into sphere-like aggregates during the aerosolizing process, rather than fractal aggregates observed from the direct emission. The particles of *B. subtilis* spores could be composed of a single spore or a cluster of spores with a sphere-like shape. As a result, the measured D_{sym} values were scattered from 0.15 to 0.83. As would be expected, the greatest variance in values was for the ambient aerosol particles. Within this population, there are more sphere-like shapes among the small sizes, whose populations are roughly split between sphere-like and irregularly shaped particles with $D_{sym} < 0.7$. As particle size increases, the population of spherical particles decrease and virtually all large particles have $D_{sym} < 0.7$. This is confirmed from a correlation analysis of over 30,000 ELS patterns from ambient aerosol particles, which show the percentages of spherical particles diminishing with increasing particle size [4].

Quantifying the asymmetry of a particle through its ELS pattern provides an additional parameter that can assist in the classification process. While *Af*, *SPX*, or D_{sym} could be valuable parameters to assist in particle differentiation, it is important to note that their value may diminish with particle size. The frequency of structure in ELS patterns increases with size, which may not be reflected in the values of these parameters, reducing their usefulness. In addition, clusters of particles may aggregate into a spherical form which may not be detectable for the shapes of their primary particles using these techniques.
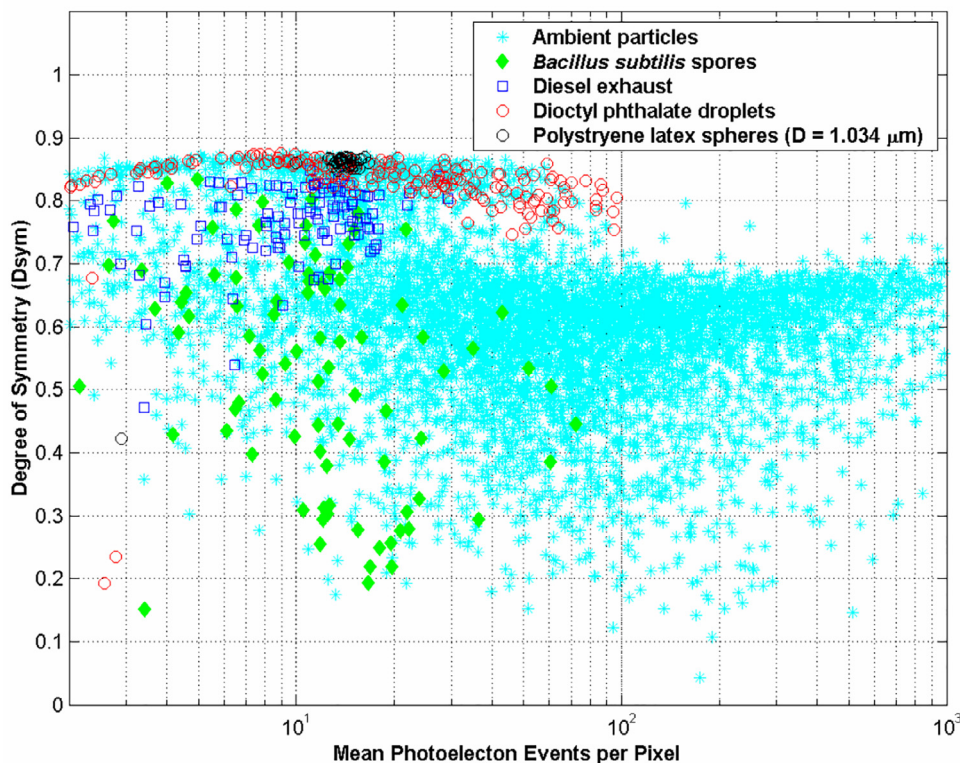
Fig. 9. D_{sym} as a function of the mean number of photoelectron events per pixel (proportional to the scattering intensity) for various aerosols having different morphologies. Reprinted from Aptowicz [2].

4.4. Surface roughness and fine structures

In addition to particle size, shape and refractive index, surface roughness can affect a particle's ELS patterns significantly. The effect of roughness can be studied theoretically by calculating the ELS Mueller matrix elements from particles with a quantifiable amount of surface roughness. One common method of doing so is to insert Gaussian roughness onto the particle. A sphere with such roughness can be specified as [95],

$$r(\theta, \phi) = r_o\left[1 + \alpha\, A e^{-\Delta\theta^2/2\sigma^2}\right] \tag{9}$$

in which the roughness is uniformly centered at randomly chosen points on the sphere surface. In this equation, r_o is the radius of the unperturbed sphere, A is a random number in the range ($-1 \le A \le 1$), so that peaks and valleys can be either outward or inward pointing; $0 \le \alpha \le 1$ is a preset parameter; $\Delta\theta$ is the relative angle between the radial vectors pointing to the center of the Gaussian peak and its reference point; and σ is the standard deviation of the Gaussian distribution used to control the size of the peaks. This type of surface roughness has also been applied to other shapes of particles [58,95,98,124,195,199].

Another type of particle that is inherently rough is the Chebyshev particles described as

$$r(\theta, \phi) = r_o[1 + \varepsilon \cos(n\theta) \cos(n\phi)] \tag{10}$$

where n is the order of the Chebyshev polynomial, and ε represents the deformation parameter. The ELS from an axisymmetric 2D or a non-axisymmetric 3D surface perturbation can be fully calculated [10,79]. While the DDA provides more flexibility in the morphologies it can address, the T-matrix solution provides greater accuracy, especially when coupled with the analytical means of calculating the light-scattering Mueller-matrix elements averaged over orientation [89,112] to compare the effects of different levels of surface roughness [79]. To perform orientation averaging with
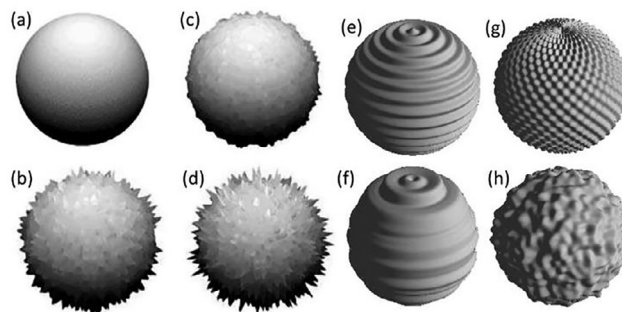

Fig. 10. (a) A spherical particle; The spherical particle was roughed at different degrees of (b)-(d) Gaussian roughness. Reprinted from Li et al. [95] with permission of Elsevier (www.elsevier.com); (e-f) 2-D Chebyshev; and (g-h) 3-D Chebyshev particles. Reprinted from Kahnert et al. [79], with permission of Elsevier (www.elsevier.com).

the DDA requires brute force, calculating the light scattering from numerous randomly selected particle orientations until the standard deviation is below a set level. The number of calculations depends greatly on particle size and shape, the particular Mueller matrix element and even the scattering angle. T-matrix methods are generally hampered by convergence issues that depend primarily on particle size and the level of surface irregularity of the particle; however, recent work to calculate the T-matrix from the shape matrix appear to be free of these issues. An analytical solution to the ELS from particles described by Chebyshev polynomials has even been developed using the *Sh*-matrix technique, which are free of the convergence issues that plague other T-matrix methodologies [142]. Fig. 10 shows the differences in these two types of roughness. The Gaussian roughness can appear much spikier than the roughness of the Chebyshev particles.
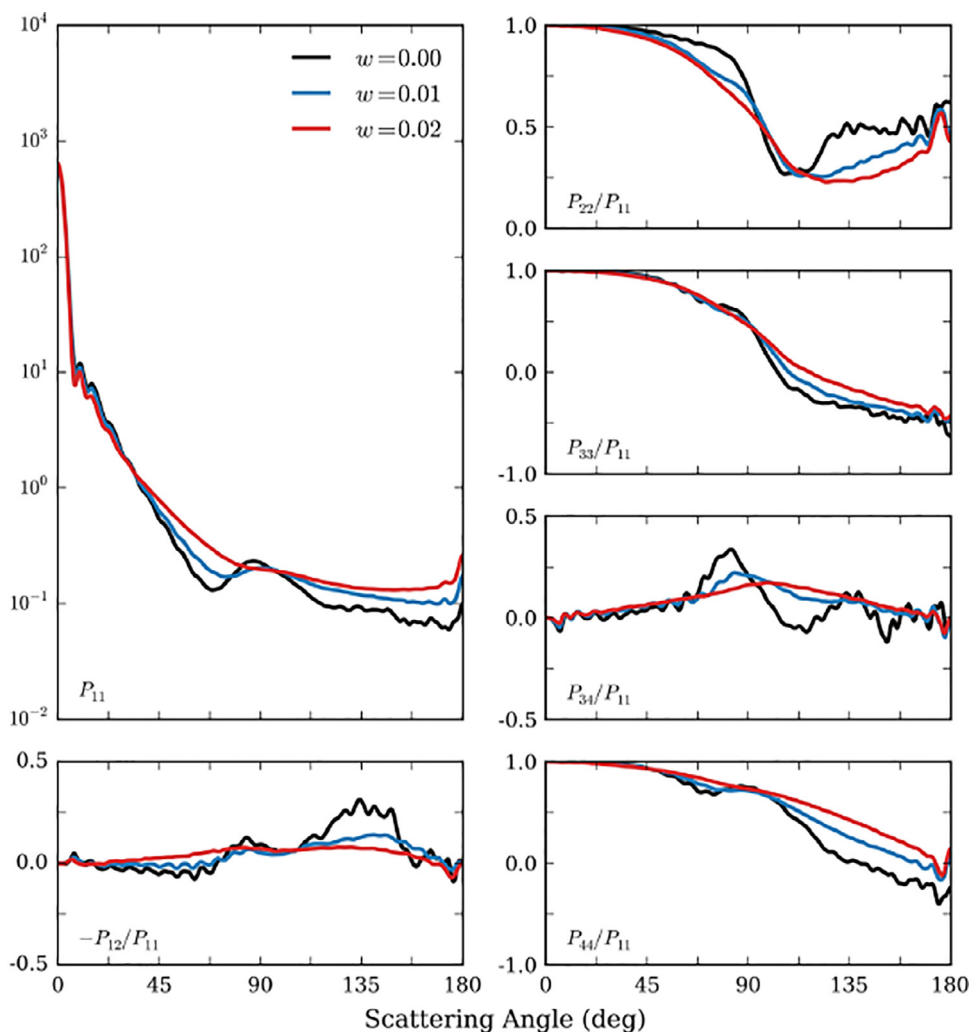
Fig. 11. Phase matrix elements computed for $ka = 50$ spheroids with different levels of surface roughness indicated by w. Reprinted from Zhang et al. [199], with permission of Elsevier (www.elsevier.com).

Based on the simulations from spheres, spheroids, hexagons, and other irregular shapes of particles with roughed surfaces [58,79,95,98,108,124,143,146,164,181,195,199], it was found that

1. The effect of surface fine structure or roughness on the ELS pattern and Mueller matrix cannot be considered independent of the initial particle. There is a nonlinear relationship dependent upon the particle's size, shape, absorption, and surface roughness. In general, the impact of surface roughness increases with the particle's size, especially in the large particle size range ($x > 20$).
2. The diffuse scatter from a rough surface smooths any sharp ELS features from those of a smooth particle of the same shape. As the roughness increases, the smoothing of the scattered field increases, lowering the relative intensity variations, and eventually resulting in relatively featureless curves for all Mueller matrix elements, particularly in the forward-scattering directions.
3. All Mueller matrix elements are more sensitive to the surface roughness in the backscattering directions. This is because the forward direction is dominated by diffraction, which is relatively insensitive to the roughness.
4. The intensity phase function $I(\theta)$, or S_{11}, is less sensitive to surface roughness than the polarization Mueller matrix elements. Therefore, it is more effective to measure polarization or depo-

larization than the intensity phase function in studying surface roughness.
5. In some cases, the surface roughness and irregularization of facial geometry generate similar influences on the scattering phase matrices as shown in the simulations for hexagonal columns.

Fig. 11 shows a typical example of the computed ELS Mueller matrix elements for spheroids with an equivalent particle size parameter $ka = 50$. It demonstrates how the matrix elements change with increasing surface roughness parameter w, which is equal to the standard deviation σ with a mean zero roughened by the Gaussian spikes described by Eq. (7) [199].

Experimentally, it is difficult to isolate the contribution of surface roughness on the observed ELS patterns from other factors, so there are limited reports about the impact of surface structure or roughness. Fig. 12 illustrates how backscattering patterns depend on surface roughness, which increases from left to right. The four particles have similar sizes, so the differences in the scattering patterns would be due predominantly to the differences in surface roughness. For the polystyrene microsphere with a smooth surface and the glass microspheres with minor surface perturbation, we see the concentric rings that we expect from spherical particles with only minor variations. When the surface roughness increases, these rings became broken and distorted. Johnson grass spores
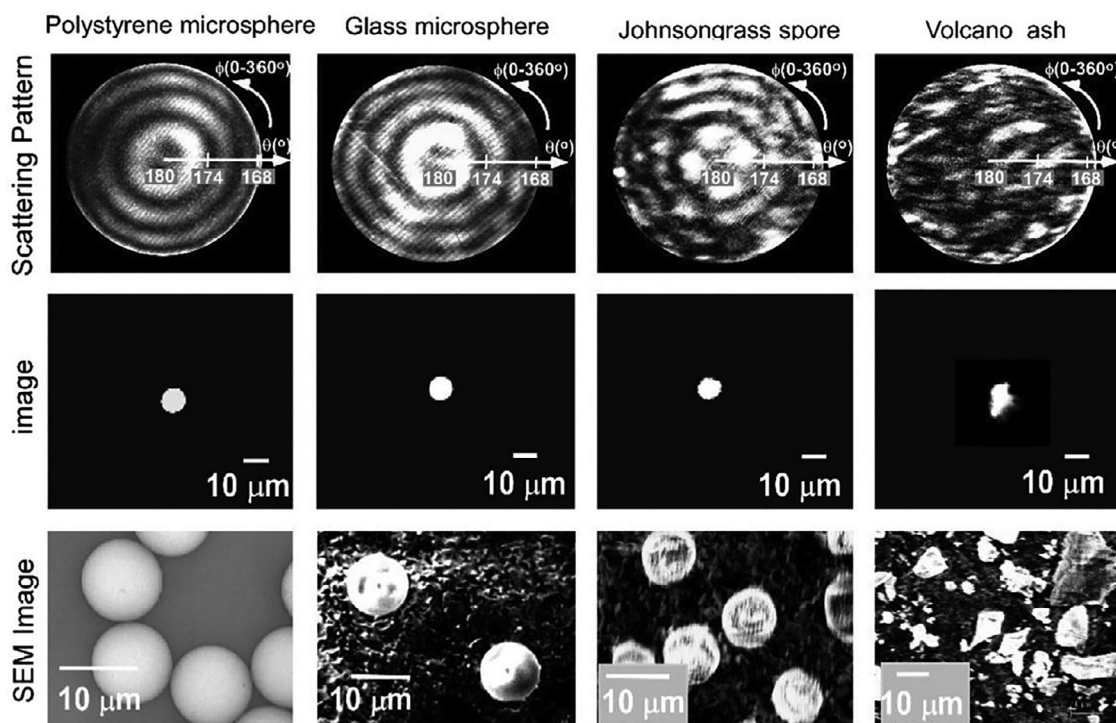
Fig. 12. Top row: Backscattered intensity patterns (θ=167.7°–180°, ϕ=0°–360°, with circular polarization 465-nm laser illumination) obtained from single laser-trapped particles with different surface roughness. Middle Row: optical images of the particles captured when the ELS pattern was recorded. Bottom Row: SEM images of the sample particles. The columns correspond to a polystyrene microsphere, a borosilicate glass microsphere, a Johnson grass spore, and a volcanic-ash particle (left to right). All particles are approximately 8 μm across. Reprinted from Fu et al. [51] with permission of Elsevier (www.elsevier.com).

have an inhomogeneous density distribution and much rougher surfaces, but largely retains a spherical shape, so the pattern still retains evidence of the concentric ring structure, but with significant intensity variations. In the very center of the pattern, we can see that the ring structure has disappeared and left islands of speckle. It appears that all three approximately spherical particles contain 4 high intensity rings along the polar scattering angle, i.e., the oscillation frequency of the scattering is dominated by the overall particle size, while the particle surface roughness contributes to strong intensity deviations along the azimuthal scattering angle, decreasing the integrated intensity of the ring and resulting in a lower-contrast phase function. These experimental results corroborate the modeling results for rough particles. Once the particle shape is far from a sphere, no more concentric rings remains as demonstrated by the volcano ash particle [51].

The influence of surface roughness on ELS patterns was also studied in observations of 8 μm sphere-like aggregates formed of polystyrene with primary 0.202, 0.988 and 2.9 μm diameter microspheres, *B. subtilis* spores, and NaCl crystals. The different primary particles formed different degrees of surface roughness, which increase with the size of the primary particles, for the aggregates with similar overall sizes. The increasing roughness also resulted in less ELS intensity difference (or features smoothing) as theoretically predicted [9].

While a spherical droplet is a relatively simple system to obtain the size by comparing the measurement with the calculation [1,65,80,152], any small deformity or impurity of a sphere distorts the ELS pattern, and makes the characterization much more difficult [164,181]. While experience allows us to see features in the ELS patterns indicating the nature of the deformity, training a computer to do this can be challenging. Haddrell et al. [64] has successfully developed such an algorithm to differentiate among four different morphologies of droplets ranging in size from 5 to 30 μm in radius: homogeneous, core/shell, with inclusions, and non-

spherical/inhomogeneous (Fig. 13). The method relies on the measurement of the near-forward scattering pattern ($32° < \theta < 58°$) of the observed droplet, and was established through the qualitative analysis of over one million individual phase functions of various particle morphologies.

4.5. Depolarization in light scattering

As discussed in the previous section, the backward scattering intensity and polarization degree are more sensitive to the change of surface roughness and morphology of the scattering particle than that in the forward direction. The linear polarization of light scattered by a particle is generally characterized by

$$P = \frac{I_\perp - I_\parallel}{I_\perp + I_\parallel} \tag{11}$$

where $I_\perp$ and $I_\parallel$ are the intensity of the scattered light polarized perpendicular and parallel within scattering plane, respectively. In the near-backward direction, the degree of linear polarization for unpolarized incident light is negative for many particles. This phenomena of negative polarization was intensively studied, and has been suggested as a means of sizing particles within an aggregate, which could also be useful in discriminating bioaerosol particles from other aerosol particles [57,155,167,168,174,200].

The ELS from aggregates composed of different oblong primary particles were calculated using the DDA to see how the negative polarization branch would depend on the shape and orientation of the primary particles. The modeling suggests that increasing the aspect ratio of the primary particles increases the amount of interaction between the particles, leading to a more prominent negative polarization branch. Decreasing the refractive index, packing density and polydispersity of the primary particles in the aggregate can reduce the amplitude of the negative polarization for these particles, as well as increasing the randomness of the particle ori-
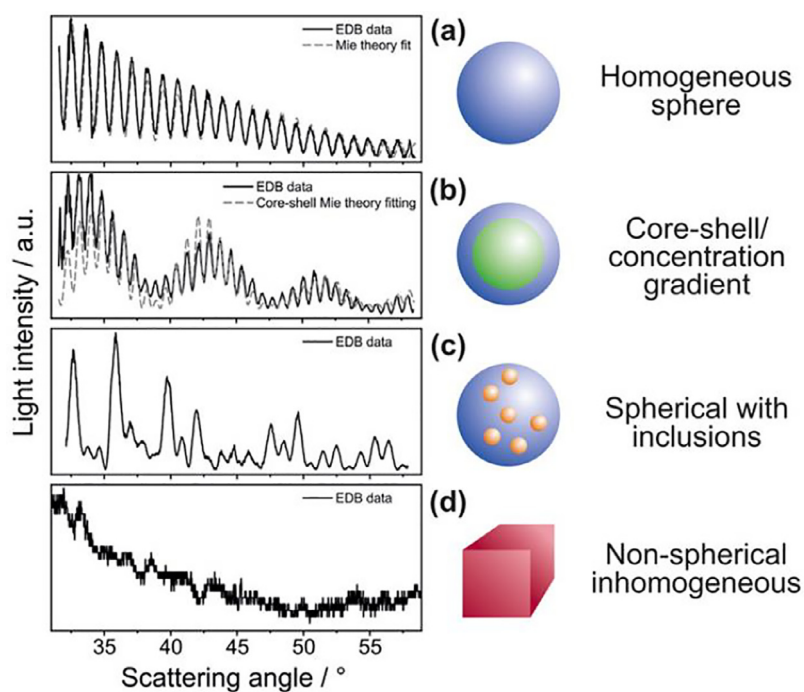
Fig. 13. Measured ELS phase functions from individual droplets composed of (a) water, (b) dodecanol-water, (c) ethylene glycol with polystyrene nanospheres, and (d) dry sodium chloride. Theoretical fitted curves are also shown in (a) and (b) in dashed-lines. Reprint from Haddrell et al. [64].
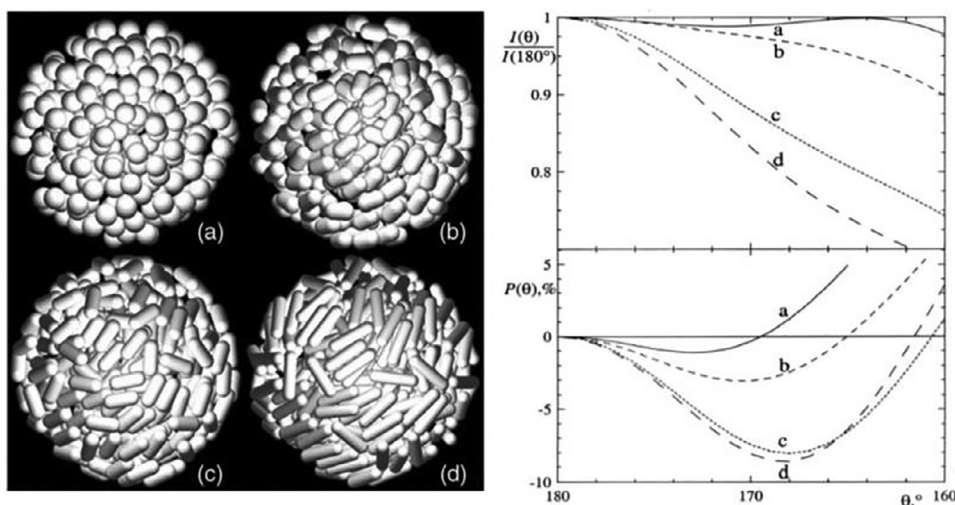

Fig. 14. (Left) Models of aggregates composed from different primary particles, all with refractive index $n = 1.59$, size parameter $x = 10$, and packing density $\rho = 0.25$. (Right) Intensity and polarization as functions of scattering angle for the corresponding aggregates. Reprinted from Zubko et al. [200] with permission of the Optical Society.

entations. The modeling also suggests that the negative polarization branch can be used to size the primary particles composed of the aggregate, which could be a valuable method for discriminating clusters of spores from other aerosol particles [200].

Experimentally measured polarized ELS distributions of aggregates composed of different primary particles in near-backward directions (155°–180°) demonstrate various degree of negative polarization (Fig. 15). The aggregates are formed from spherical PSL microspheres, *B. subtilis* spores, Arizona road dust, and tryptophan particles. The experimental results suggest that the degree of negative polarization is more pronounced in more densely packed aggregates as predicted in the theoretical calculation. These results indicate that the polarization in the near-backward direction could be used as a fingerprint to discriminate aggregates having differences in their constituent primary particles [58,155,167,174,200], or to classify different irregular shapes of particles and bioaerosol

particles [23,24,96,139,169]. The depolarization is also a key parameter in atmospheric LIDAR applications. The single particle results obtained in the laboratory could be useful in the interpretation of LIDAR observations for the detection and characterization of airborne bioaerosol particles [29,159,194].

4.6. Circular intensity differential scattering (CIDS) and helix structure in DNA

In this section, we discuss measurements of circular polarization, specifically the circular intensity differential scattering (CIDS), i.e. the normalized Mueller matrix element $-S_{14}/S_{11}$, which has exhibited an ability in detecting cells and spores, even discriminating between different species and strains [26–28,136,166,169,189].
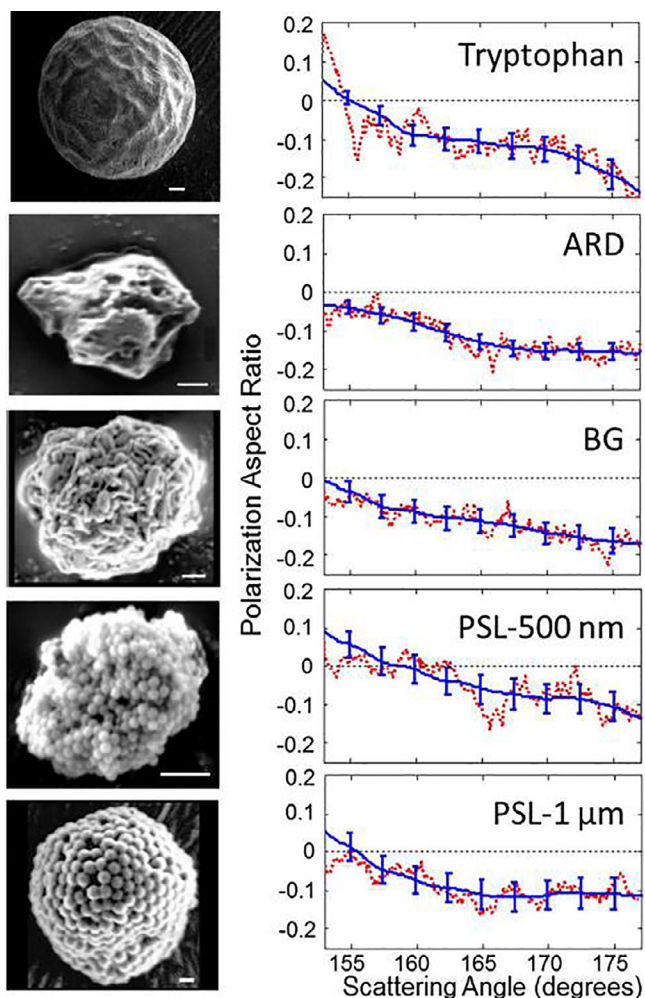
Fig. 15. (Left) Sample SEM images of 5 aggregates composed of different primary particles. The scale bar is 1 μm. (Right) Averaged linear polarization (S_{12}/S_{11}) of the aggregates from 200 measurements. The red dotted lines represent the experimental data, and the solid line is a smoothed fit along the polar angle (θ). The error bars indicate the 95% confidence interval after averaging over 200 aggregates. Reprinted from Redding et al. [155] with permission of the Optical Society.

For right- and left-hand circularly polarized light input in Eq. (3), the **S** vector incident on the system is $\begin{bmatrix} 1 \\ 0 \\ 0 \\ 1 \end{bmatrix}$ and $\begin{bmatrix} 1 \\ 0 \\ 0 \\ -1 \end{bmatrix}$, respectively. Then, the output intensity after illumination of the circularly polarized light is $I_{\text{out},R} = S_{11} + S_{14}$ and $I_{\text{out},L} = S_{11} - S_{14}$, respectively. The resulting

$$CIDS = -S_{14}/S_{11} = (I_{out,L} - I_{out,R})/(I_{out,L} + I_{out,R}) \qquad (12)$$

CIDS measurements were reported to be able to distinguish chiral properties in particles, whether they be material or structural as the helix structures of DNA molecules in biological systems. Such measurements for CIDS or Mueller matrix elements were carried out using the polarization modulation technique developed by Hunt and Huffman [75,76]. Because the polarization is modulated, typically at 10 s of kilohertz, a finite amount of time is required to take these measurements. This technique has been used to measure the ELS from static systems, like substrates, particles in suspension, or in a group of aerosol particles, but to date, there is no report that the matrix element was obtained from a single aerosol particle in a flow.

There has been a long history in the study of helical structures using the measurement of matrix element S_{14} or CIDS [45,75]. The CIDS ($-S_{14}/S_{11}$) measurements on suspensions of helical sperm cells of *Eledone cirrhosa* provide information on the long-range chiral structures of samples in solution [104,165,166,189]. These experimental results are in reasonably good agreement with theoretical simulations based on the first Born approximation [189], or coupled-dipole approximation [166]. The Born approximation supplied a simple method for calculating S_{14}, but had difficulty in obtaining other matrix elements accurately. While the coupled-dipole approximation model had broader applicability in calculating all matrix elements [165,166]. Fig. 16 shows similarly distinguishable features of the results from the two research groups.

Another application of CIDS measurements showed the study of intracellular polymerization of hemoglobin S in the suspensions of sickle cells, which demonstrated that the S_{14} amplitude increases with deoxyhemoglobin concentration, and S_{14} was able to be used to estimate the effect of oxygen tension, cell density, and osmotic stress on intracellular hemoglobin polymerization [56]. The combined measurements of S_{14} and S_{34} could supply more geometric parameters of the super-helical structures in nucleosomes, chromatin and nuclei, which were extracted from rat hepatocytes [42]. The differential distinction (scattering + absorption) intensity from right- and left-hand circularly polarized light at different deep UV wavelengths was also used to study biological macro-structures, the circular dichroism measurements on the disrupted T2 virus suspensions, and purified T2 phage DNA. They showed high sensitivity on the detection of the special geometry [45].

Although CIDS has shown the ability to detect the chiral properties often indicative of biological systems for about half a century [45,75], there is limited advancement and application since these initial studies. One key barrier is the requirement for precise optical components and highly accurate alignments in the experiment, as well as being able to measure the very weak signals. CIDS intensity was estimated to be in the order of 10^{-3} to 10^{-6} for most biological systems, so the sum of polarization anisotropy caused by the light source, optical components, and any artificial effects produced during the light and signal-propagating processes including the detector itself must be controlled to be well below 1%, and it is extremely difficult to correct system error through the calibration process [189]. Nevertheless, without considering the polarization anisotropy caused by other optical surfaces, the ellipticity, i.e. $(I_{\text{max}} - I_{\text{min}})/(I_{\text{max}} + I_{\text{min}})$ of the circularly polarized light could be $\geq$ 1.2% for the best commercially available quarter-wave plate with a retardation tolerance of $\lambda/500$, assuming perfect alignment can be achieved. The quarter-wave plate is the optical component required to produce circularly polarized light from a linearly polarized light beam, $\lambda/500$ retardation tolerance will cause $|\delta - 90| \geq 0.72°$, which is equivalent with an ellipticity of 1.2%, where δ is the retardance of the wave plate. This shows how challenging it is to constrain the polarization anisotropy to below 1% experimentally and provide an effective measurement of CIDS.

4.7. Algorithms for discriminating bioaerosol from other aerosol particles

Aerosol particle properties of size, shape, fine structure and composition can provide distinctive ELS features that may provide a means of distinguishing and detecting bioaerosol particles. Various algorithms have been developed to classify particles using the ELS measurements, for instance, using Fourier transforms, auto-correlations, multivariate analyses, and machine learning [39,44,72,128,130,131,149,147,186].

The purpose behind Fourier and correlation analyses is to try to extract frequencies of high-intensity scattering peaks of particles to obtain deviations of the complex frequencies from an equiva-
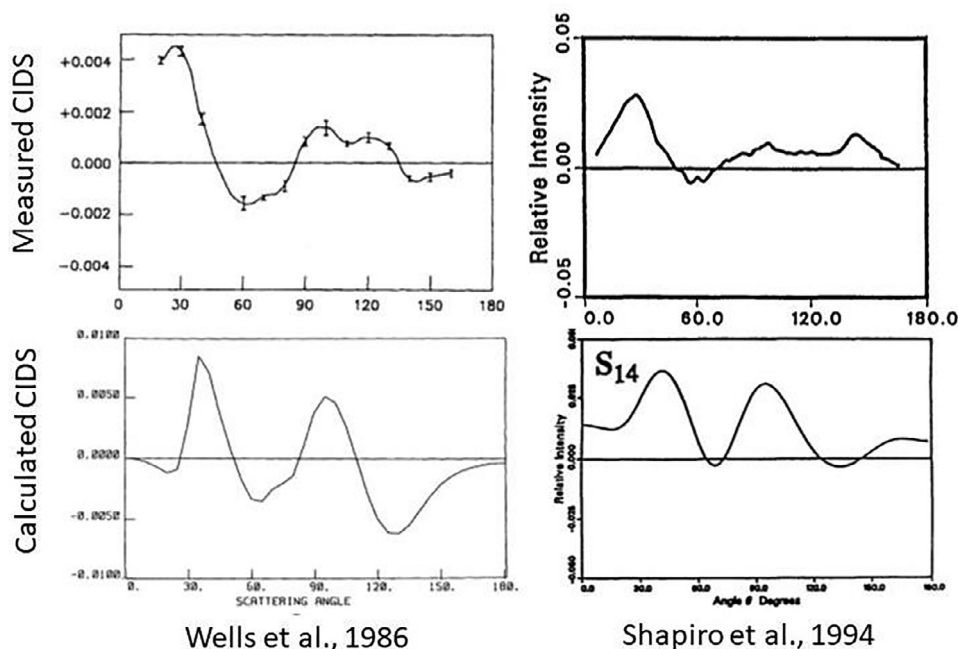
Fig. 16. Similarly distinguishable CIDS features from experimental measurements and theoretical simulations of sperm cells of *Eledone cirrhosa*. Reprinted from Wells et al. [189] and Shapiro et al. [166] with permission of The Optical Society.
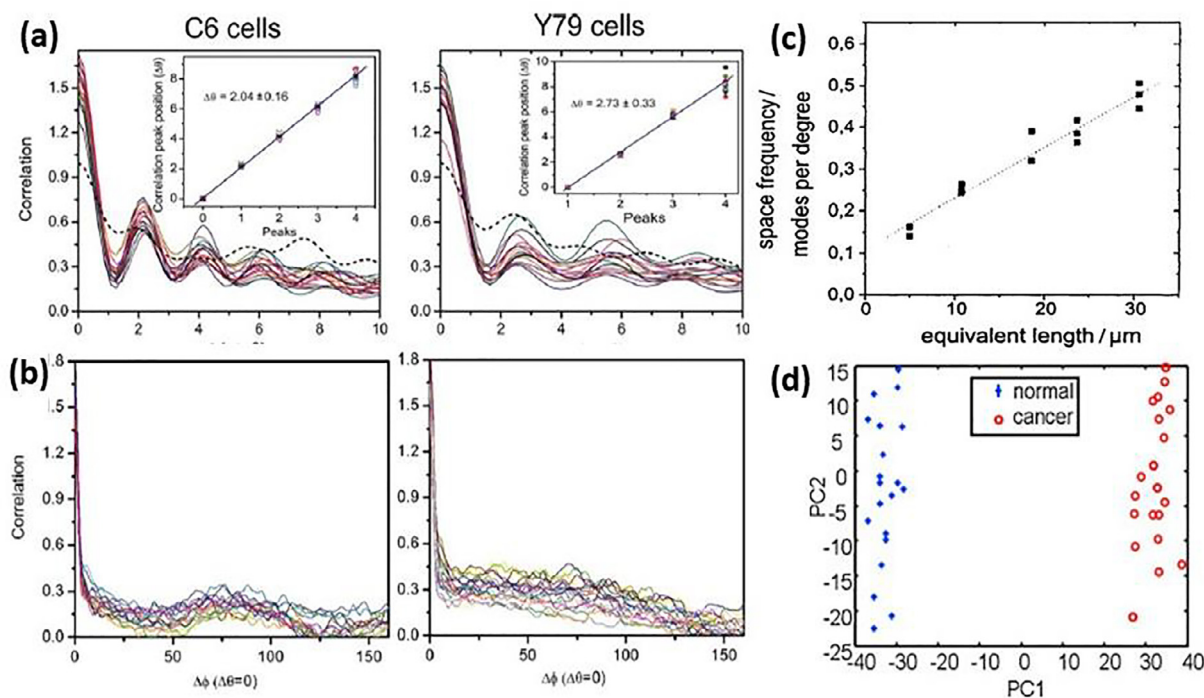

Fig. 17. (a)-(b) Autocorrelation from the ELS patterns of 16 individual C6 and Y79 cells as a function of $\Delta\theta$ at $\Delta\phi=0$ and $\Delta\phi$ at $\Delta\theta=0$, respectively. The inset shows the correlation peak positions vary from cell to cell as $\Delta\theta$ increases. (c) The spatial frequency of scattering peaks from solid NaCl particles at various sizes as a function of the equivalent edge length of a cube. (d) Scattering plot of the first two principal components of confocal back scattering spectra of a normal cell and cancerous cell. Reprinted from Pan *et al.* [130], Berge *et al.* [14], and Wang *et al.* [185].

lent sphere to estimate the non-sphericity of arbitrary-shaped particles. The resulting size and shape information is used to discriminate aerosol particles from each other [e.g. 14,25,38,130,150,158]. Fig. 17(a)-(b) shows the autocorrelation parameters extracted from the individual ELS patterns obtained from two kinds of cells. The results demonstrate classification of cells in a label-free flow cytometry by autocorrelation analysis. Although the two kinds of cells are hard to distinguish by their morphologies and ELS patterns using visual examination directly [130], they are easily distin-

guishable through the autocorrelation analysis. Fig. 17(c) shows a Fourier analysis results of solid NaCl particles at different sizes and demonstrates a linear relationship between the spatial frequency of the scattering peaks per angle and the equivalent edge length of the NaCl cube [14].

Multivariate techniques, such as principal component analysis (PCA), extract information from large sets of data by minimizing data redundancy, but keeping the most important information. In PCA, a set of reduced variables obtained from a large matrix of
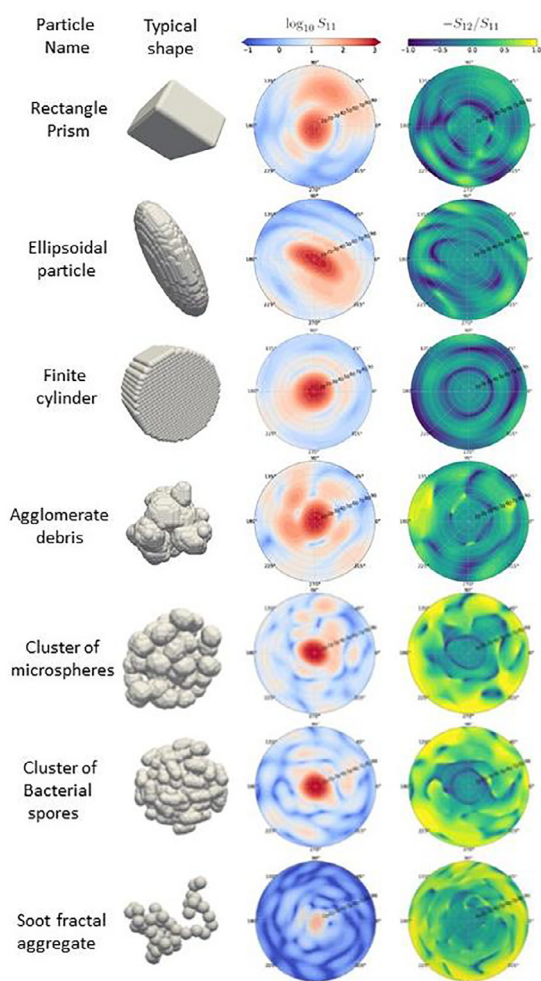
Fig. 18. Calculated ELS intensity S_{11} (in logarithmic scale) and the degree of linear polarizations $-S_{12}/S_{11}$ ($0° \leq \theta \leq 90°$, $0° \leq \phi \leq 360°$) for particles of a typical rectangular prism, ellipsoid, cylinder, aggregate debris, cluster of microspheres, cluster of bacterial spores, and soot fractal aggregate. All particles have a volume-equivalent size parameter $x = 5$, refractive index $n = 1.5 + i0$, and are illuminated by unpolarized light. Reprinted from Piedra et al. [149] with permission of Elsevier (www.elsevier.com).

correlated data are generated. This new orthogonal principal component data, which are eigenvectors of the covariance matrix of the original data set, is in fact a linear combination of the original variables. The application of PCA works much better at recognizing large sets of high dimensional data in this new coordinate projection formed by orthogonal principal components, which indicates the data in terms of the differences and similarities between them [127]. Fig. 17(d) shows a notable example that normal cells and cancerous cells are well-discriminated via PCA analysis from their confocal back scattering spectra [185].

With increased computational capabilities and development of mathematical algorithms, machine learning (ML) has greatly improved pattern recognition capabilities. ML technology has been widely used for pathologic analysis in the medical field [55,103], morphological classification of galaxies in astronomy [30], discrimination in land cover [126], and the classification of ELS patterns [39,44,148,149]. The classification of ELS patterns through ML is a process of image information extraction followed by sorting. First, the ML algorithm is provided with a training set to extract common features from a group of patterns that are measured or calculated from a group of similar scattering particles (e.g. a group of *B. subtilis* particles), as well as all common features from other

individual groups of aerosol particles (e.g. groups of pollen, dust, soot, aggregates of atmospheric aerosol particles). The ML algorithm identifies common representative features among patterns from the different individual groups, especially the target group of bioaerosol particles from the other groups (e.g. *B. subtilis* against others). This training procedure is generally based on an established mathematical and computational algorithm such as convolutional neural networks or successive subspace learning, which have demonstrated accurate classification for 2D and 3D datasets [92,148,149]. Once this training procedure is finished, a complete database and a classification algorithm are created which can be used to classify unknown aerosol particles. Any measured ELS pattern is compared with the known features extracted from the different groups of aerosol particles in the database to examine and evaluate which group it belongs to most closely.

ML has been tested using different scattering properties, including different elements of the Mueller matrix. Piedra et al. [148,149] generated 1070 model particles in each of 7 different morphological groups (total 7×1070 particles): rectangular prisms (boxes), ellipsoids, finite cylinders, aggregate debris, clusters of microspheres, clusters of bacterial spores, and soot fractal aggregates. The 1070 particles in each group had randomized dimensions and orientations relative to the illuminating light, but retained the same volume-equivalent size parameter $x = 5$, and refractive index $n = 1.5 + i0$. The ELS Mueller-matrix intensity ($0° \leq \theta \leq 180°$, $0° \leq \phi \leq 360°$) were calculated for all particles. Fig. 18 shows a typical calculated pattern (S_{11} and $-S_{12}/S_{11}$) in the forward direction ($0° \leq \theta \leq 90°$, $0° \leq \phi \leq 360°$) for each group of particles. Based on the calculated patterns, 70 sets of S_{11} and $-S_{12}/S_{11}$ from each group were randomly selected as the training set for computer training based on a convolutional neural network learning procedure. The trained neural network was then presented with 1000 data sets from each particle group for examination and classification. The results turned out to be very promising: the classification accuracies were approximately 99% for the regularly shaped particles (rectangular prism, ellipsoid, and cylinder) and above 97% for the highly irregularly shaped particles (other four groups). For the clusters resembling bacterial spores, in particular, classification accuracy reached better than 99% [148]. Similar classification accuracies were obtained when the total intensity S_{11} and polarization element S_{12} were used. Piedra et al. [148] used class activation mapping to identify the locations in the ELS pattern from which the classifications were made. Interestingly, the class activations mapping revealed different types of particles utilized different portions of the ELS patterns. For instance, unsurprisingly, classifications of all particles based on the total scattered intensity were made predominantly from the forward-scattering region; however, classifications using matrix element S_{12} utilized the mid-range scattering angles of the scattering patterns to classify the sphere and spore clusters. The forward scattering is dominated by diffraction, which is responsive to particle shape; whereas the mid-range scattering angles are more sensitive to roughness features. The aggregated spheres and clusters have similar overall shape, but their surface roughness has different spatial characteristics.

Performing ML on imagery captured through ELS experiments has many complications that do not exist in modeling. Experimental data always includes unexpected artificial fluctuations and noise from the light source, detector, optical components, and position of particle to the illuminating light that creates the ELS signal. For instance, in the training process the same class of particle is introduced into the system repeatedly to collect a training dataset. If there is any minor artificial fluctuation from the measurements, for example caused by a random reflection of stray light, it could mix with the ELS signal. Any artifacts in the measurements can result in a less accurate classification of the observed patterns than for the modeled particles, as the ML algorithm may distinguish
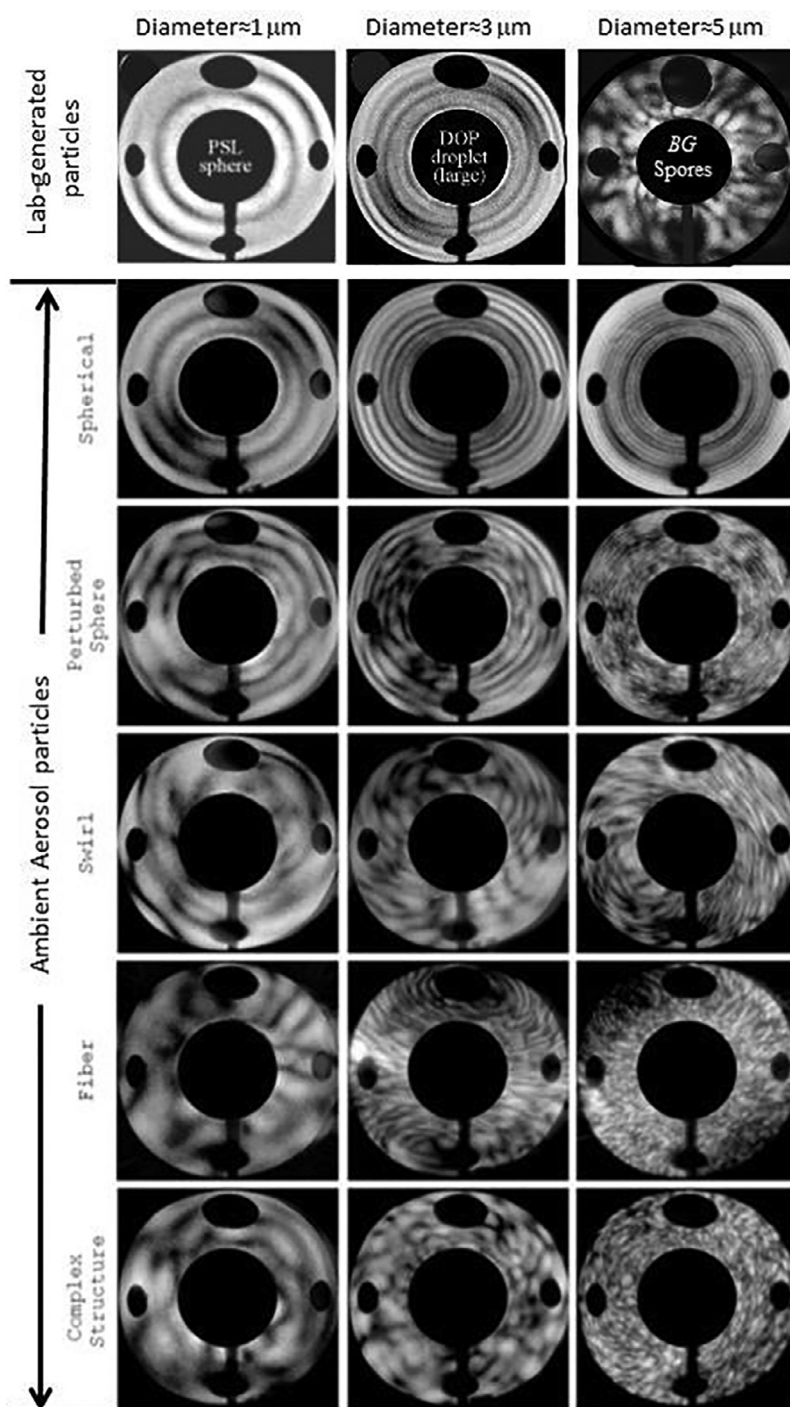
Fig. 19. Measured ELS patterns ($75° \leq \theta \leq 135°$, $0° \leq \phi \leq 360°$) from single aerosol particles having different sizes (increasing from ∼1 μm to ∼5 μm, left to right) including laboratory-generated particles (top row): single PSL microsphere (1.034 μm), dioctyl phthalate droplet (∼3 μm), and aggregate of *B. subtilis* spores (∼5 μm), and various ambient aerosol particles (rows 2–6). Reprinted from Aptowicz [2] and Aptowicz et al. [5] with permission of John Wiley and Sons (www.wiley.com).

the particles based on these artifacts rather than the ELS signal. Despite these complications, ML has extracted features using discrete cosine Fourier transform and some nonlinear operations on more than 3000 measured ELS intensity patterns ($75° \leq \theta \leq 135°$, $0° \leq \phi \leq 360°$). These patterns were measured from individual aerosol particles in the size range of 1–50 μm in size. The interrogated particles for the study were primarily sampled ambient aerosol particles with the addition of laboratory generated particles such as single or small clusters of *B. subtilis* spores, PSL microspheres (1.034 μm), droplets of dioctyl phthalate, particulate matter in diesel exhaust, and Arizona road dust [2,39]. Fig. 19 shows typical patterns from these particles. The aim of the classification process was to discriminate patterns of *B. subtilis* from other ambient airborne aerosol particles and interferents such as diesel soot particles. Although the patterns were extremely diverse and complicated, especially those from the real ambient aerosol particles, it resulted in only 20% false-negative and 11% false-positive rates for the assignment of particles composed of *B. subtilis* spores [39]. The results suggest that ML is a very promising technique for bioaerosol classification. The authors also suggest additional re-

search necessary to reduce the false classifications, like incorporating the use of multiple Mueller matrix elements simultaneously [148] and the incorporation of fluorescence and Raman signatures with the ELS information [84,131,132].

5. Summary

Because of the large scattering cross-section and relatively simple and inexpensive instrumentation, ELS has been widely used in real-time analysis for the detection and characterization of aerosol particles, in both point and remote-sensing systems. ELS is sensitive to a number of parameters including particle size and shape, orientation and position related to the illuminating light, surface roughness or fine structure, the size and shape of the primary particles or molecules that form and aggregate, the distribution or packing of the primary particles or molecules within the particle, and the complex refractive index including real refractive index and absorption. Different techniques have had varying degrees of success in retrieving these parameters from ELS measurements. Since the ELS signal is non-unique, it will be necessary to incorporate other information, such as fluorescence and Raman scattering, in order to make accurate classifications or characterizations of aerosol particles with more chemical information, especially in bioaerosol sensing. While initial ML programs appear promising, it is a major task to train such algorithms with experimental data, it might be requisite to do this for every instrument separately. While a great number of studies have been made over the last five decades, the study of ELS from bioaerosols is still in its infancy.

Declaration of Competing Interest

The authors (Yong-Le Pan, Kevin Aptowicz, Jessica Arnold, Samuel Cheng, Aimable Kalume, Patricio Piedra, Chuji Wang, Joshua Santarpia, and Gorden Videen) declare that they have no known competing financial interests or personal relationships that could have appeared to influence the work reported in this paper.

Acknowledgements

References

[1] Anand S, Eryurek M, Karadag Y, Erten A, Serpenguzel A, Jonas A, Kiraz A. Observation of whispering gallery modes in elastic light scattering from microdroplets optically trapped in a microfluidic channel. J Opt Soc Am B-Opt Phys 2016;33(7):1349–54. doi:10.1364/Josab.33.001349.

[2] Aptowicz, K. (2005). Angularly-resolved elastic light scattering of microparticles, Ph.D Dissertation. https://www.wcupa.edu/sciences-mathematics/physics/kAptowicz/documents/Thesis_Aptowicz.pdf.

[3] Aptowicz KB, Pan YL, Chang RK, Pinnick RG, Hill SC, Tober RL, Goyal A, Leys T, Bronk BV. Two-dimensional angular optical scattering patterns of microdroplets in the mid infrared with strong and weak absorption. Opt Lett 2004;29(17):1965–7. doi:10.1364/Ol.29.001965.

[4] Aptowicz KB, Pan YL, Martin SD, Fernandez E, Chang RK, Pinnick RG. Decomposition of atmospheric aerosol phase function by particle size and asphericity from measurements of single particle optical scattering patterns. J Quant Spectrosc Radiat Transf 2013;131:13–23. doi:10.1016/j.jqsrt.2013.03.020.

[5] Aptowicz KB, Pinnick RG, Hill SC, Pan YL, Chang RK. Optical scattering patterns from single urban aerosol particles at Adelphi, Maryland, USA: a classification relating to particle morphologies. J Geophys Res-Atmosph 2006;111(D12) Artn D12212. doi:10.1029/2005jd006774.

[6] Ashkin A, Dziedzic JM. Observation of resonances in the radiation pressure on dielectric spheres. Phys Rev Lett 1977;38:1351–4.

[7] Ashkin A, Dziedzic JM. Observation of LS from nonspherical particles using optical levitation. Appl Opt 1980;19(5):660–8. doi:10.1364/Ao.19.000660.

[8] Ashkin A, Dziedzic JM. Observation of optical resonances of dielectric spheres by light scattering. Appl Opt 1981;20:1803–14.

[9] Auger JC, Aptowicz KB, Pinnick RG, Pan YL, Chang RK. Angularly resolved light scattering from aerosolized spores: observations and calculations. Opt Lett 2007;32(22):3358–60. doi:10.1364/Ol.32.003358.

[10] Auger JC, Fernandes GE, Aptowicz KB, Pan YL, Chang RK. Influence of surface roughness on the elastic-light scattering patterns of micron-sized aerosol particles. Appl Phys B-Lasers Opt 2010;99(1–2):229–34. doi:10.1007/s00340-010-3914-0.

[11] Barnes MD, Lermer N, Whitten WB, Ramsey JM. A CCD based approach to high-precision size and refractive index determination of levitated microdroplets using Fraunhofer diffraction. Rev Sci Instrum 1997;68:2287–91.

[12] Bartholdi M, Salzman GC, Hiebert RD, Kerker M. Differential LS photometer for rapid analysis of single particles in flow. Appl Opt 1980;19(10):1573–81. doi:10.1364/Ao.19.001573.

[13] Bell BW, Bickel WS. Single fiber light scattering matrix: an experimental determination. Appl Opt 1981;20(22):3874–9. doi:10.1364/AO.20.003874.

[14] Berge B, Sudholz K, Steiner B, Rohmann J, Ruhl E. In situ size determination of single levitated solid aerosols. Phys Chem Chem Phys 1999;1(24):5485–9.

[15] Berne BJ, Pecora R. Dynamic light scattering. Courier Dover Publications; 2000.

[16] Bickel WS, Davidson JF, Huffman DR, Kilkson R. Application of polarization effects in light scattering: a new biophysical tool. Proc Natl Acad Sci USA 1976;73:486–90.

[17] Bickel WS, Stafford ME. Polarized light scattering from biological systems: a technique for cell differentiation. J Biol Phys 1981;9:53–66.

[18] Bickel WS, Bailey WM. Stokes vectors, mueller matrices, and polarized scattered-light. Am J Phys 1985;53(5):468–78. doi:10.1119/1.14202.

[19] Bickel WS, Yousif HA, Bailey WM. Masking of information in light scattering signals from complex scatterers. Aerosol Sci Technol 1982;1(3):329–35. doi:10.1080/02786828208958598.

[20] Bickel WS, Videen G. Stokes vectors, mueller matrices and polarized scattered-light - experimental applications to optical-surfaces and all other scatterers. Opt Scatter 1991;1530:7–14. doi:10.1117/12.50491.

[21] Bohren C, Huffman DR. Absorption and scattering of light by small particles. WILEY-VCH Verlag GmbH & Co KGaA; 1998.

[22] Bottiger JR, Voss KJ, Fry ES. Polarized light scattering by small particles. Aerosol Sci Technol 1982;1(3):317–27. doi:10.1080/02786828208958597.

[23] Bronk BV, Druger SD, Czege J, Vandemerwe WP. Measuring diameters of rod-shaped bacteria in-vivo with polarized-light scattering. Biophys J 1995;69(3):1170–7. doi:10.1016/S0006-3495(95)79991-X.

[24] Bronk BV, Van de Merwe WP, Stanley M. In vivo measure of average bacterial cell size from a polarized light scattering function. Cytometry 1992;13(2):155–62. doi:10.1002/cyto.990130208.

[25] Brunel M, Coëtmellec S, Gréhan G, Delobel T. Determination of the size of irregular particles using interferometric out-of-focus imaging. Int J Opt 2014;143904. doi:10.1155/2014/143904.

[26] Bustamante C, Maestre MF, Tinoco I. Circular intensity differential scattering of light by helical structures .1. theory. J Chem Phys 1980;73(9):4273–81. doi:10.1063/1.440709.

[27] Bustamante C, Maestre MF, Tinoco I. Circular intensity differential scattering of light by helical structures .2. Applications. J Chem Phys 1980;73(12):6046–55. doi:10.1063/1.440139.

[28] Bustamante C, Tinoco I, Maestre MF. Circular intensity differential scattering of light by helical structures .3. A general polarizability tensor and anomalous scattering. J Chem Phys 1981;74(9):4839–50. doi:10.1063/1.441736.

[29] Cao XY, Roy G, Bernier R. Lidar polarization discrimination of bioaerosols. Opt Eng 2010;49(11) Artn 116201. doi:10.1117/1.3505877.

[30] Cheng TY, Conselice CJ, Aragon-Salamanca A, Li N, Bluck AFL, Hartley WG, Annis J, Brooks D, Doel P, Garcia-Bellido J, Kuehn N, Kuropatkin N, Smith M, Sobreira F, Tarle G. Optimizing automatic morphological classification of galaxies with machine learning and deep learning using Dark Energy Survey imaging. Mon Not R Astron Soc 2020;493(3):4209–28. doi:10.1093/mnras/staa501.

[31] Cholleton D, Bialic E, Dumas A, Kaluzny P, Rairoux P, Miffre A. Laboratory evaluation of the scattering matrix of ragweed, ash, birch and pine pollens towards pollen classification. Atmos Measure Tech 2021. doi:10.5194/amt-2021-272.

[32] Chýlek P. Large-sphere limits of the Mie scattering functions. J Opt Soc Am 1973;63:699–716.

[33] Chýlek P. Partial wave resonances and the ripple structure of the Mie normalized extinction cross section. J Opt Soc Am 1976;66:285–7.

[34] Chýlek P, Kiehl JT, Ko MKW. Optical levitation and partial wave resonances. Phys Rev A 1978;18:2229–33.

[35] Chýlek P, Kiehl JT, Ko MKW. Narrow resonance structure in the Mie scattering characteristics. Appl Opt 1978;17:3019–21.

[36] Chýlek P, Videen G. Longwave radiative properties of polydispersed hexagonal ice crystals. J Atmos Sci 1994;51:175–90.

[37] Chýlek P, Videen G. Scattering by a composite sphere and effective medium approximations. Opt Comm 1998;146:15–20.

[38] Cleuvenbergen SV, Smith ZJ, Deschaume O, Bartic C, Wachsmann-Hogiu S, Verbiest T, Van Der Veen MA. Morphology and structure of ZIF-8 during crystallisation measured by dynamic angleresolved second harmonic scattering. Nat Commun 2018;9:3418.

[39] Crosta GF, Zomer S, Pan YL, Holler S. Classification of single-particle two-dimensional angular optical scattering patterns and heuristic scatterer reconstruction. Opt Eng 2003;42(9):2689–701. doi:10.1117/1.1599840.

[40] Debye P. Zerstreuung von Röntgenstrahlen. Ann Phys 1915;351(6):809–23. doi:10.1002/andp.19153510606.

[41] Descartes R. Discours de la méthode pour bien conduire sa raison et chercher la vérité dans les sciences. la dioptrique. les météores et la géometrie. Leyde, France; 1637. 2nd appendix.

[42] Diaspro A, Bertolotto M, Vergani L, Nicolini C. Polarized-light scattering of nucleosomes and polynucleosomes - insitu and invitro studies. IEEE Trans Biomed Eng 1991;38(7):670–8. doi:10.1109/10.83568.

[43] Dick WD, Ziemann PJ, Huang PF, McMurry PH. Optical shape fraction measurements of submicrometre laboratory and atmospheric aerosols. Measure Sci Technol 1998;9(2):183–96. doi:10.1088/0957-0233/9/2/006.

[44] Ding CZ. Convolutional neural networks for particle shape classification using LS patterns. J Quant Spectrosc Radiat Transf 2020;245:106901.

[45] Dorman BP, Maestre MF. Experimental differential LS correction to the circular dichroism of bacteriophage T2. Proc Nat Acad Sci 1973;70(1):255–9. doi:10.1073/pnas.70.1.255.

[46] Draine BT. The discrete-dipole approximation and its application to interstellar graphite grains. Astrophys J 1988;333(2):848–72. doi:10.1086/166795.

[47] Dubovik O, Holben BN, Lapyonok T, Sinyuk A, Mishchenko MI, Yang P, Slutsker I. Non-spherical aerosol retrieval method employing light scattering by spheroids. Geophys Res Lett 2002;29(10):1415 Artn 1415. doi:10.1029/2001 gl014506.

[48] Dubovik O, Sinyuk A, Lapyonok T, Holben BN, Mishchenko M, Yang P, Eck TF, Volten H, Muñoz O, Veihelmann B, van der Zande WJ, Leon J-F, Sorokin M, Slutsker I. Application of spheroid models to account for aerosol particle non-sphericity in remote sensing of desert dust. J Geophys Res 2006;111:D11208. doi:10.1029/2005JD006619.

[49] Ebert M, Weinbruch S, Rausch A, Gorzawski G, Hoffmann P, Wex H, Helas G. Complex refractive index of aerosols during LACE 98 as derived from the analysis of individual particles. J Geophys Res-Atmosp 2002;107(D21) Artn 8121. doi:10.1029/2000jd000195.

[50] Fernandes GE, Pan YL, Chang RK, Aptowicz K, Pinnick RG. Simultaneous forward- and backward-hemisphere elastic-LS patterns of respirable-size aerosols. Opt Lett 2006;31(20):3034–6. doi:10.1364/Ol.31.003034.

[51] Fu R, Wang CJ, Munoz O, Videen G, Santarpia JL, Pan YL. Elastic backscattering patterns via particle surface roughness and orientation from single trapped airborne aerosol particles. J Quant Spectrosc Radiat Transf 2017;187:224–31. doi:10.1016/j.jqsrt.2016.09.018.

[52] Gans R. Strahlungsdiagramme ultramikroskopischer Teilchen. Ann Phys 1925;381(1):29–38. doi:10.1002/andp.19253810103.

[53] Gilliar Wolfgang, Bickel W, Bailey W. Light diffraction studies of single muscle fibers as a function of fiber rotation. Biophys J 1984;45:1159–65. doi:10.1016/S0006-3495(84)84264-2.

[54] Gómez Martín JC, Guirado D, Frattin E, Bermudez-Edo M, Cariñanos Gonzalez P, Olmo Reyes FJ, Nousiainen T, Gutiérrez PJ, Moreno F, Muñoz. On the application of scattering matrix measurements to detection and identification of major types of airborne aerosol particles: volcanic ash, desert dust and pollen. J Quant Spectrosc Radiat Transf 2021;271:107761.

[55] Grist JT, Withey S, MacPherson L, Oates A, Powell S, Novak J, Abernethy L, Pizer B, Grundy R, Bailey S, Mitra D, Arvanitis TN, Auer DP, Avula S, Peet AC. Distinguishing between paediatric brain tumour types using multi-parametric magnetic resonance imaging and machine learning: a multi-site study. Neuroimage-Clin 2020;25:102172 ARTN 102172. doi:10.1016/j.nicl.2020.102172.

[56] Gross CT, Salamon H, Hunt AJ, Macey RI, Orme F, Quintanilha AT. Hemoglobin polymerization in sickle cells studied by circular polarized-light scattering. Biochim Biophys Acta 1991;1079(2):152–60. doi:10.1016/0167-4838(91)90120-O.

[57] Grynko Y, Shkuratov Y, Forstner J. Light scattering by irregular particles much larger than the wavelength with wavelength-scale surface roughness. Opt Lett 2016;41(15):3491–4. doi:10.1364/Ol.41.003491.

[58] Grynko Y, Shkuratov Y, Forstner J. Intensity surge and negative polarization of light from compact irregular particles. Opt Lett 2018;43(15):3562–5. doi:10.1364/Ol.43.003562.

[59] Gu YL, Hu YH, Zhao XY, Chen X. Determination of infrared complex refractive index of microbial materials. J Quant Spectrosc Radiat Transf 2018;217:305–14. doi:10.1016/j.jqsrt.2018.06.011.

[60] Gucker FT, Egan JJ. Measurement of angular variation of light scattered from single aerosol droplets. J Colloid Sci 1961;16(1):68. doi:10.1016/0095-8522(61)90064-2.

[61] Gucker FT, Okonski CT, Pickard HB, Pitts JN. A photoelectronic counter for colloidal particles. J Am Chem Soc 1947;69(10):2422–31. doi:10.1021/ja01202a053.

[62] Gucker FT, Tůma J, Lin H-M, Huang C-M, Ems SC, Marshall TR. Rapid measurement of LS diagrams from single particles in an aerosol stream and determination of latex particle size. J Aerosol Sci 1973;4(5):389–404. doi:10.1016/0021-8502(73)90028-1.

[63] Hadamcik E, Renard J-B, Levasseur-Regourd AC, et al. Light scattering by aggregates: interconnecting size and absorption effects (PROGRA(2) experiment). J Quant Spectrosc Radiat Transf 2009;110(14–16) SI1755-SI1770.

[64] Haddrell A, Rovelli G, Lewis D, Church T, Reid J. Identifying time-dependent changes in the morphology of an individual aerosol particle from its light scattering pattern. Aerosol Sci Technol 2019;53(11):1334–51. doi:10.1080/02786826.2019.1661351.

[65] Hart MB, Sivaprakasam V, Eversole JD, Johnson LJ, Czege J. Optical measurements from single levitated particles using a linear electrodynamic quadrupole trap. Appl Opt 2015;54(31):F174–81.

[66] Heinson YW, Maughan JB, Heinson WR, Chakrabarti A, Sorensen CM. Light scattering Q-space analysis of irregularly shaped particles. J Geophys Res-Atmos 2016;121(2):682–91. doi:10.1002/2015jd024171.

[67] Henning U, Rehn K, Hoehn B. Cell envelope and shape of Escherichia-Coli-K12. Proc Natl Acad Sci USA 1973;70(7):2033–6. doi:10.1073/pnas.70.7.2033.

[68] Heyder J, Gebhart J. Optimization of response functions of LS instruments for size evaluation of aerosol-particles. Appl Opt 1979;18(5):705–11. doi:10.1364/Ao.18.000705.

[69] Holler S, Auger JC, Stout B, Pan YL, Bottiger JR, Chang RK, Videen G. Observations and calculations of light scattering from clusters of spheres. Appl Opt 2000;39(36):6873–87 10.1364/Ao.39.006873.

[70] Holler S, Fuerstenau SD, Skelsey CR. Simultaneous two-color, two-dimensional angular optical scattering patterns from airborne particulates: scattering results and exploratory analysis. J Quant Spectrosc Radiat Transf 2016;178:167–75. doi:10.1016/j.jqsrt.2016.01.009.

[71] Holler S, Pan YL, Chang RK, Bottiger JR, Hill SC, Hillis DB. Two-dimensional angular optical scattering for the characterization of airborne microparticles. Opt Lett 1998;23(18):1489–91. doi:10.1364/Ol.23.001489.

[72] Holler S, Zomer S, Crosta GF, Pan YL, Chang RK, Bottiger JR. Multivariate analysis and classification of two-dimensional angular optical scattering patterns from aggregates. Appl Opt 2004;43(33):6198–206. doi:10.1364/Ao.43.006198.

[73] Hudson PK, Gibson ER, Young MA, Kleiber PD, Grassian VH. Coupled infrared extinction and size distribution measurements for several clay components of mineral dust aerosol. J Geophys Res 2008(D1):113. doi:10.1029/2007JD008791.

[74] Huffman JA, Perring AE, Savage NJ, Clot B, Crouzy B, Tummon F, Shoshanim O, Damit B, Schneider J, Sivaprakasam V, Zawadowicz MA, Crawford I, Gallagher M, Topping D, Doughty DC, Hill SC, Pan YL. Real-time sensing of bioaerosols: review and current perspectives. Aerosol Sci Technol 2020;54(5):465–95. doi:10.1080/02786826.2019.1664724.

[75] Hunt AJ, Huffman DR. A new polarization-modulated light scattering instrument. Rev Sci Instrum 1973;44(12):1753–62. doi:10.1063/1.1686049.

[76] Hunt AJ, Huffman DR. A polarization-modulated light scattering instrument for determining liquid aerosol properties. Jpn J Appl Phys 1975;14(S1):435. doi:10.7567/jjaps.14s1.435.

[77] Jacobsen RT, Kerker M, Matijevic E. Aerosol Studies by light scattering. V. Preparation and particle size distribution of aerosol consisting of particles exhibiting high optical absorption. J Phys Chem 1967;71(3):514.

[78] Jones LJF, Carballido-Lopez R, Errington J. Control of cell shape in bacteria: helical, actin-like filaments in Bacillus subtilis. Cell 2001;104(6):913–22. doi:10.1016/S0092-8674(01)00287-2.

[79] Kahnert M, Nousiainen T, Thomas MA, Tyynela J. Light scattering by particles with small-scale surface roughness: comparison of four classes of model geometries. J Quant Spectrosc Radiat Transf 2012;113(18):86–97. doi:10.1016/j.jqsrt.2012.03.017.

[80] Kalume A, Beresnev LA, Santarpia J, Pan YL. Detection and characterization of chemical aerosol using laser-trapping single-particle Raman spectroscopy. Appl Opt 2017;56(23):6577–82. doi:10.1364/Ao.56.006577.

[81] Kaye P, Hirst E, WangThomas Z. Neural-network-based spatial LS instrument for hazardous airborne fiber detection. Appl Opt 1997;36(24):6149–56. doi:10.1364/Ao.36.006149.

[82] Kaye PH. Spatial LS analysis as a means of characterizing and classifying non-spherical particles. Measur Sci Technol 1998;9(2):141–9. doi:10.1088/0957-0233/9/2/002.

[83] Kaye PH, AlexanderBuckley K, Hirst E, Saunders S, Clark JM. A real-time monitoring system for airborne particle shape and size analysis. J Geophys Res-Atmos 1996;101(D14):19215–21. doi:10.1029/96jd00228.

[84] Kaye PH, Barton JE, Hirst E, Clark JM. Simultaneous light scattering and intrinsic fluorescence measurement for the classification of airborne particles. Appl Opt 2000;39(21):3738–45. doi:10.1364/Ao.39.003738.

[85] Kaye PH, Eyles NA, Ludlow IK, Clark JM. An instrument for the classification of airborne particles on the basis of size, shape, and count frequency. Atmos Environ Part a-General Top 1991;25(3–4):645–54. doi:10.1016/0960-1686(91)90062-C.

[86] Kaye PH, Hirst E, Clark JM, Micheli F. Airborne particle-shape and size classification from spatial LS profiles. J Aerosol Sci 1992;23(6):597–611. doi:10.1016/0021-8502(92)90027-S.

[87] Kaye PH, Stanley WR, Hirst E, Foot EV, Baxter KL, Barrington SJ. Single particle multichannel bio-aerosol fluorescence sensor. Opt Express 2005;13(10):3583–93. doi:10.1364/Opex.13.003583.

[88] Kerker M. Light scattering instrumentation for aerosol studies: an historical overview. Aerosol Sci Technol 1997;27(4):522–40. doi:10.1080/02786829708965492.

[89] Khlebtsov NG. Orientational averaging of light-scattering observables in the T-matrix approach. Appl Opt 1992;31:5359–65.

[90] Kinnunen M, Kauppila A, Karmenyan A, Myllyla R. Effect of the size and shape of a red blood cell on elastic light scattering properties at the single-cell level. Biomed Opt Express 2011;2(7):1803–14. doi:10.1364/Boe.2.001803.

[91] Krieger UK, Marcolli C, Reid JP. Exploring the complexity of aerosol particle properties and processes using single particle techniques. Chem Soc Rev 2012;41(19):6631–62. doi:10.1039/c2cs35082c.

[92] Kuo CCJ, Zhang M, Li SY, Duan JL, Chen YR. Interpretable convolutional neural networks via feedforward design. J Vis Commun Image Represent 2019;60:346–59. doi:10.1016/j.jvcir.2019.03.010.

[93] Lane PA, Hart MB, Jain V, Tucker JE, Eversole JD. Characterization of single particle aerosols by elastic light scattering at multiple wavelengths. J Quant Spectrosc Radiat Transf 2018;208:188–95. doi:10.1016/j.jqsrt.2017.12.017.

[94] Laven, P. MiePlot: a computer program for scattering of light from a sphere using Mie theory & Debye series. Retrieved from http://www.philiplaven.com/mieplot.htm

[95] Li CH, Kattawar GW, Yang P. Effects of surface roughness on light scattering by small particles. J Quant Spectrosc Radiat Transf 2004;89(1–4):123–31. doi:10.1016/j.jqsrt.2004.05.016.

[96] Li D, Chen F, Zeng N, Qiu ZG, He HH, He YH, Ma H. Study on polarization scattering applied in aerosol recognition in the air. Opt Express 2019;27(12):A581–95. doi:10.1364/Oe.27.00a581.

[97] Lim J, Ding H, Mir M, Zhu R, Tangella K, Popescu G. Born approximation model for light scattering by red blood cells. Biomed Opt Express 2011;2(10):2784–91.

[98] Liu C, Panetta RL, Yang P. The effective equivalence of geometric irregularity and surface roughness in determining particle single-scattering properties. Opt Express 2014;22(19):23620–7. doi:10.1364/Oe.22.023620.

[99] Lorenz L. Videnskab. Selskab. Skrifter 1890;6:142 Reprinted in Lorenz, L. (1896). Oeuvres Scientiques, Librairie Lehmann, Copenhagen, Vol. I, pp. 405-502.

[100] Lu JQ, Yang P, Hu XH. Simulations of light scattering from a biconcave red blood cell using the finite-difference time-domain method. J Biomed Opt 2005;10(2):024022 Artn 024022. doi:10.1117/1.1897397.

[101] Macke A, Mueller J, Raschke E. Single scattering properties of atmospheric ice crystals. J Atmos Sci 1996;53(19):2813–25. doi:10.1175/1520-0469(1996)053⟨2813:Sspoai⟩2.0.Co;2.

[102] Mackowski DW, Mishchenko MI. A multiple sphere T-matrix Fortran code for use on parallel computer clusters. J Quant Spectrosc Radiat Transf 2011;112(13):2182–92. doi:10.1016/j.jqsrt.2011.02.019.

[103] Madabhushi A, Lee G. Image analysis and machine learning in digital pathology: challenges and opportunities. Med Image Anal 2016;33:170–5. doi:10.1016/j.media.2016.06.037.

[104] Maestre MF, Bustamante C, Hayes TL, Subirana JA, Tinoco I. Differential scattering of circularly polarized-light by the helical sperm head from the Octopus Eledone-Cirrhosa. Nature 1982;298(5876):773–4. doi:10.1038/298773a0.

[105] Maetzler C. Research report. Vienna, Austria; 2002. retrieved from.

[106] Martins JV, Artaxo P, Liousse C, Reid JS, Hobbs PV, Kaufman YJ. Effects of black carbon content, particle size, and mixing on light absorption by aerosols from biomass burning in Brazil. J Geophys Res-Atmos 1998;103(D24):32041–50. doi:10.1029/98jd02593.

[107] Martín JGG, Guirado D, Frattin EM, Gonzalez PC, Nousiainen T, Gutiérrez PJ, Moreno F, Muñoz O. On the application of scattering matrix measurements to detection and identification of major types of airborne aerosol particles: volcanic ash, desert dust and pollen. J Quant Spectrosc Radiat Transf 2021;271:107761.

[108] Mehri T, Kemppinen O, David G, Lindqvist H, Tyynela J, Nousiainen T, Rairoux P, Miffre A. Investigating the size, shape and surface roughness dependence of polarization lidars with LS computations on real mineral dust particles: application to dust particles' external mixtures and dust mass concentration retrievals. Atmos Res 2018;203:44–61. doi:10.1016/j.atmosres.2017.11.027.

[109] Mie G. Contributions on the optics of turbid media, particularly colloidal metal solution (P. newman, trans.) annalen der physik, 25. Greifswald: Physikalishes Institut; 1908. p. 377–445.

[110] Miffre A, Cholleton D, Rairoux P. Laboratory evaluation of the scattering matrix elements of mineral dust particles from 176.0 degrees up to 180.0 degrees-exact backscattering angle. J Quant Spectrosc Radiat Transf 2019;222:45–59. doi:10.1016/j.jqsrt.2018.10.019.

[111] Millikan RA. A new modification of the cloud method of determining the elementary electrical charge and the most probable value of that charge. Philosoph Mag 1910;19(109–14):209–28. doi:10.1080/14786440208636795.

[112] Mishchenko MI. Light scattering by randomly oriented axially symmetric particles. J Opt Soc Am A 1991;8:871–82.

[113] Mishchenko MI. Comprehensive thematic T-matrix reference database: a 2017-2019 update. J Quant Spectrosc Radiat Transf 2020;242:106692 UNSP 106692. doi:10.1016/j.jqsrt.2019.106692.

[114] Mishchenko MI, Travis LD. Capabilities and limitations of a current FORTRAN implementation of the T-matrix method for randomly oriented, rotationally symmetric scatterers. J Quant Spectrosc Radiat Transf 1998;60(3):309–24. doi:10.1016/S0022-4073(98)00008-9.

[115] Mishchenko MI, Travis LD, Mackowski DW. T-matrix computations of light scattering by nonspherical particles: a review. J Quant Spectrosc Radiat Transf 1996;55(5):535–75. doi:10.1016/0022-4073(96)00002-7.

[116] Muñoz O, Moreno F, Guirado D, Ramos DL, López A, Girela F, Jerónimo JM, Costillo LP, Bustamante I. Experimental determination of scattering matrices of dust particles at visible wavelengths: the IAA light scattering apparatus. J Quant Spectrosc Radiat Transf 2010;111(1):187–96.

[117] Muñoz O, Moreno F, Guirado D, Dabrowsk DD, Volten H, Hovenier JW. The Amsterdam–Granada light scattering database. J Quant Spectrosc Radiat Transf 2012;113(7):565–74.

[118] Muñoz O, Volten H, Hovenier JW, Nousiainen T, Muinonen K, Guirado D, Moreno F, Waters LBFM. Scattering matrix of large Saharan dust particles: experiments and computations. J. Geophys. Res. 2007;112:D13215.

[119] Muñoz O, Moreno F, Guirado D, Ramos JL, Volten H, Hovenier JW. The IAA Cosmic Dust Laboratory: experimental scattering matrices of clay particles. Icarus 2007;211:894–900.

[120] Ngo D, Pinnick RG. Suppression of scattering resonances in inhomogeneous microdroplets. J Opt Soc Am A 1994;11(4):1352–9. doi:10.1364/JOSAA.11.001352.

[121] Nicodemus F. Directional reflectance and emissivity of an opaque surface. Appl Opt 1965;4(7):767–75.

[122] Nieminen TA, Rubinsztein-Dunlop H, Heckenberg NR. Calculation of the T-matrix: general considerations and application of the point-matching method. J Quant Spectrosc Radiat Transf 2003;79:1019–29. doi:10.1016/S0022-4073(02)00336-9.

[123] Nouri SA, Gregory DA, Fuller K. Development of an angle-scanning spectropolarimeter: preliminary results. J Quant Spectrosc Radiat Transf 2018;206:342–54. doi:10.1016/j.jqsrt.2017.11.024.

[124] Nousiainen T, Muinonen K. Surface-roughness effects on single-scattering properties of wavelength-scale particles. J Quant Spectrosc Radiat Transf 2007;106(1–3):389–97. doi:10.1016/j.jqsrt.2007.01.024.

[125] Owen JF, Chang RK, Barber PW. Morphology-dependent resonances in raman-scattering, fluorescence emission, and elastic-scattering from microparticles. Aerosol Sci Technol 1982;1(3):293–302. doi:10.1080/02786828208958595.

[126] Pal M, Maxwell AE, Warner TA. Kernel-based extreme learning machine for remote-sensing image classification. Remote Sens Lett 2013;4(9):853–62. doi:10.1080/2150704x.2013.805279.

[127] Pan YL, Eversole JD, Kaye PH, Foot V, Pinnick RG, Hill SC, Mayo MW, Bottiger JR, Huston A, Sivaprakasam V, Chang RK. Bioaerosol fluorescence. Dordrecht; 2007.

[128] Pan YL. Detection and characterization of biological and other organic-carbon aerosol particles in atmosphere using fluorescence. J Quant Spectrosc Radiat Transf 2015;150:12–35. doi:10.1016/j.jqsrt.2014.06.007.

[129] Pan YL, Aptowicz KB, Chang RK, Hart M, Eversole JD. Characterizing and monitoring respiratory aerosols by light scattering. Opt Lett 2003;28(8):589–91. doi:10.1364/Ol.28.000589.

[130] Pan YL, Berg MJ, Zhang SSM, Noh H, Cao H, Chang RK, Videen G. Measurement and autocorrelation analysis of two-dimensional LS patterns from living cells for label-free classification. Cytometry Part A 2011;79a(4):284–92. doi:10.1002/cyto.a.21036.

[131] Pan YL, Hill SC, Pinnick RG, House JM, Flagan RC, Chang RK. Dual-excitation-wavelength fluorescence spectra and elastic scattering for differentiation of single airborne pollen and fungal particles. Atmos Environ 2011;45(8):1555–63. doi:10.1016/j.atmosenv.2010.12.042.

[132] Pan YL, Hill SC, Pinnick RG, Huang H, Bottiger JR, Chang RK. Fluorescence spectra of atmospheric aerosol particles measured using one or two excitation wavelengths: comparison of classification schemes employing different emission and scattering results. Opt Express 2010;18(12):12436–57. doi:10.1364/Oe.18.012436.

[133] Pan YL, Hill SC, Santarpia JL, Brinkley K, Sickler T, Coleman M, Williamson C, Gurton K, Felton M, Pinnick RG, Baker N, Eshbaugh J, Hahn J, Smith E, Alvarez B, Prugh A, Gardner W. Spectrally-resolved fluorescence cross sections of aerosolized biological live agents and simulants using five excitation wavelengths in a BSL-3 laboratory. Opt Express 2014;22(7):8165–89. doi:10.1364/Oe.22.008165.

[134] Pan YL, Holler S, Chang RK, Hill SC, Pinnick RG, Niles S, Bottiger JR. Single-shot fluorescence spectra of individual micrometer-sized bioaerosols illuminated by a 351- or a 266-nm ultraviolet laser. Opt Lett 1999;24(2):116–18. doi:10.1364/Ol.24.000116.

[135] Pan YL, Wang CJ, Beresnev LA, Yuffa AJ, Videen G, Ligon D, Santarpia JL. Measurement of back-scattering patterns from single laser trapped aerosol particles in air. Appl Opt 2017;56(3):B1–4. doi:10.1364/Ao.56.0000b1.

[136] Patterson CW, Singham SB, Salzman GC, Bustamante C. Circular intensity differential scattering of light by hierarchical molecular-structures. J Chem Phys 1986;84(3):1916–21. doi:10.1063/1.450441.

[137] Patterson HS, Gray RW. The scattering of light by the individual particles in smokes. Proc R Soc London Ser a-Contain Papers Math Phys Character 1926;113(764):312–22. doi:10.1098/rspa.1926.0157.

[138] Perry RJ, Hunt AJ, Huffman DR. Experimental determinations of mueller scattering matrices for nonspherical particles. Appl Opt 1978;17(17):2700–10. doi:10.1364/Ao.17.002700.

[139] Pezzaniti JL, Chipman RA. Mueller matrix imaging polarimetry. Opt Eng 1995;34(6):1558–68. doi:10.1117/12.206161.

[140] Petrov D, Synelnyk E, Shkuratov Yu, Videen G. The T-matrix technique for calculations of scattering properties of ensembles of randomly oriented particles with different size. J Quant Spectrosc Radiat Transf 2006;102:85–110.

[141] Petrov D, Synelnyk E, Shkuratov YG, Videen G, Scotto C, Hart M, Eversole J. Photopolarimetric properties of analytic models of some biological particles with irregular shape. J Quant Spectrosc Radiat Transf 2006;102:111–20.

[142] Petrov D, Shkuratov Y, Videen G. Analytical LS solution for Chebyshev particles. J Opt Soc Am A 2007;24:1103–1119.

[143] Petrov D, Shkuratov Y, Videen G. Influence of corrugation on LS properties of capsule and finite-cylinder particles: analytic solution using Sh-matrices. J Quant Spectrosc Radiat Transf 2008;109:650–69.

[144] Petrov D, Shkuratov Yu, Videen G. Application of the Sh-matrices method to light scattering by spheroids. J Opt 2010;12:095701. doi:10.1088/2040-8978/12/9/095701.

[145] Petrov D, Shkuratov Yu, Videen G. Electromagnetic wave scattering from particles of arbitrary shapes. J Quant Spectrosc Radiat Transf 2011;112:1636–45.

[146] Petrov D, Shkuratov Yu, Videen G. Light scattering by arbitrary shaped particles with rough surfaces: sh-matrices approach. J Quant Spectrosc Radiat Transf 2012;113:136–48.

[147] Petrov D. Photopolarimetrical properties of coronavirus model particles: spike proteins number influence. J Quant Spectrosc Radiat Transf 2020;248:107005. doi:10.1016/j.jqsrt.2020.107005.

[148] Piedra P, Gobert C, Kalume A, Pan YL, Kocifaj M, Muinonen K, Penttila A, Zubko E, Videen G. Where is the machine looking? Locating discriminative LS features by class-activation mapping. J Quant Spectrosc Radiat Transf 2020;247:106936 ARTN 106936UNSP. doi:10.1016/j.jqsrt.2020.106936.

[149] Piedra P, Kalume A, Zubko E, Mackowski D, Pan YL, Videen G. Particle-shape classification using light scattering: an exercise in deep learning. J Quant Spectrosc Radiat Transf 2019;231:140–56. doi:10.1016/j.jqsrt.2019.04.013.

[150] Popov KA, Kurzweg TP. Light scattering by ellipsoidal particles and Fourier analysis in the frequency domain. In: Proc. SPIE 7187, Biomedical Applications of Light Scattering; 2009. III.

[151] Prahl, S., & Jaques, S. Mie Scattering. Retrieved from https://omlc.org/software/mie/

[152] Preston TC, Reid JP. Determining the size and refractive index of microspheres using the mode assignments from Mie resonances. J Opt Soc Am a-Opt Image Sci Vis 2015;32(11):2210–17. doi:10.1364/Josaa.32.002210.

[153] Purcell EM, Pennypacker CR. Scattering and absorption of light by nonspherical dielectric grains. Astrophys J 1973;186(2):705–14. doi:10.1086/152538.

[154] Rayleigh L. On the electromagnetic theory of light. Lond, Edinb, Dublin Philosop Mag J Sci 1881;12(73):81–101. doi:10.1080/14786448108627074.

[155] Redding B, Pan YL, Wang CJ, Cao H. Polarization-resolved near-backscattering of airborne aggregates composed of different primary particles. Opt Lett 2014;39(14):4076–9. doi:10.1364/Ol.39.004076.

[156] Reyes FL, Jeys TH, Newbury NR, Primmerman CA, Rowe GS, Sanchez A. Bioaerosol fluorescence sensor. Field Anal Chem Technol 1999;3(4–5):240–8. doi:10.1002/(Sici)1520-6521(1999)3:4/5⟨240::Aid-Fact3⟩3.0.Co;2-#.

[157] Robinson NH, Allan JD, Huffman JA, Kaye PH, Foot VE, Gallagher M. Cluster analysis of WIBS single-particle bioaerosol data. Atmos Meas Tech 2013;6(2):337–47. doi:10.5194/amt-6-337-2013.

[158] Romanova AV, Konokhovaa AI, Yastrebovaa ES, Gileva KV, Strokotova DI, Maltseva VP, Yurkin MA. Sensitive detection and estimation of particle non-sphericity from the complex Fourier spectrum of its light-scattering profile. J Quant Spectrosc Radiat Transf 2019;235:317–31.

[159] Roy G, Cao XY, Bernier R. On linear and circular depolarization LIDAR signatures in remote sensing of bioaerosols: experimental validation of the Mueller matrix for randomly oriented particles. Opt Eng 2011;50(12) Artn 6001. doi:10.1117/1.3657505.

[160] Sachweh B, Barthel H, Polke R, Umhauer H, Buttner H. Particle shape and structure analysis from the spatial intensity pattern of scattered light using different measuring devices. J Aerosol Sci 1999;30(10):1257–70. doi:10.1016/S0021-8502(99)00045-2.

[161] Sachweh BA, Dick WD, Mcmurry PH. Distinguishing between spherical and nonspherical particles by measuring the variability in Azimuthal LS. Aerosol Sci Technol 1995;23(3):373–91. doi:10.1080/02786829508965321.

[162] Savage NJ, Krentz CE, Konemann T, Han TT, Mainelis G, Pohlker C, Huffman JA. Systematic characterization and fluorescence threshold strategies for the wideband integrated bioaerosol sensor (WIBS) using size-resolved biological and interfering particles. Atmos Meas Tech 2017;10(11):4279–302. doi:10.5194/amt-10-4279-2017.

[163] Scattport. Scattport database, "Light Scattering Softwares". Retrieved from https://scattport.org/index.php/LS-software

[164] Secker DR, Kaye PH, Greenaway RS, Hirst E, Bartley DL, Videen G. Light scattering from deformed droplets and droplets with inclusions. I. Experimental results. Appl Opt 2000;39(27):5023–30. doi:10.1364/Ao.39.005023.

[165] Shapiro DB, Hunt AJ, Quinbyhunt MS, Maestre MF, Hull PG, Kaheng K. A theoretical and experimental-study of polarized-light scattering by helices. Ocean Optics Xi 1992;1750:56–72. doi:10.1117/12.140687.

[166] Shapiro DB, Mestre MF, Mcclain WM, Hull PG, Shi Y, Quinbyhunt MS, Hearst JE, Hunt AJ. Determination of the average orientation of dna in the octopus sperm eledone-cirrhossa through polarized-light scattering. Appl Opt 1994;33(24):5733–44. doi:10.1364/Ao.33.005733.

[167] Shkuratov Y, Ovcharenko A, Zubko E, Volten H, Munoz O, Videen G. The negative polarization of light scattered from particulate surfaces and of independently scattering particles. J Quant Spectrosc Radiat Transf 2004;88(1–3):267–84. doi:10.1016/j.jqsrt.2004.03.029.

[168] Sivaprakasam V, Czege J, Eversole JD. Wavelength resolved polarized elastic scatter measurements from micron sized single particles,⟩ Chmical, Biological, Radiological, Radiological, Nuclear, and explosives (CBRNE) Sensing XIV. Proc SPIE 2013;8710:871018.

[169] Sloot PMA, Hoekstra AG, Vanderliet H, Figdor CG. Scattering matrix-elements of biological particles measured in a flow through system - theory and practice. Appl Opt 1989;28(10):1752–62. doi:10.1364/Ao.28.001752.

[170] Sorensen CM. Q-space analysis of scattering by particles: a review. J Quant Spectrosc Radiat Transf 2013;131:3–12. doi:10.1016/j.jqsrt.2012.12.029.

[171] Sorensen CM, Heinson YW, Heinson WR, Maughan JB, Chakrabarti A. Q-space analysis of the light scattering phase function of particles with any shape. Atmosphere (Basel) 2017;8(4):6810 ARTN 6810.3390/atmos8040068.

[172] Sorensen CM, Lu N, Cai J. Fractal cluster-size distribution measurement using static LS. J Colloid Interface Sci 1995;174(2):456–60. doi:10.1006/jcis.1995.1413.

[173] Sun WB, Videen G, Fu Q, Hu YX. Scattered-field FDTD and PSTD algorithms with CPML absorbing boundary conditions for light scattering by aerosols. J Quant Spectrosc Radiat Transf 2013;131:166–74.

[174] Tyynelä J, Zubko E, Muinonen K, Videen G. Interpretation of single-particle negative polarization at intermediate scattering angles. Appl Opt 2010;49(28):5284–96. doi:10.1364/Ao.49.005284.

[175] Ulanowski Z, Hirst E, Kaye PH, Greenaway R. Retrieving the size of particles with rough and complex surfaces from two-dimensional scattering patterns. J Quant Spectrosc Radiat Transf 2012;113(18):187–94. doi:10.1016/j.jqsrt.2012.06.019.

[176] Van de Hulst HC. Light scattering by small particles. New York: Dover Publications, Inc; 1981.

[177] Van de Merwe WP, Huffman DR, Bronk BV. Reproducibility and sensitivity of polarized light scattering for identifying bacterial suspensions. Appl Opt 1989;28:5052–7.

[178] Van De Merwe WP, Bronk BV. Polarized light scattering as a means of detecting heat and UV-induced changes in bacteria and bacterial spores. Proc SPIE 1989;1884:202–7.

[179] Videen G, Li J, Chýlek P. Resonances and poles of weakly absorbing spheres. J Opt Soc Am A 1995;12(5):916–21.

[180] Videen G, Ngo D. Light scattering multipole solution for a cell. J Biomed Opt 1998;3(2):212–20. doi:10.1117/1.429877.

[181] Videen G, Sun WB, Fu Q, Secker DR, Greenaway RS, Kaye PH, Hirst E, Bartley D. Light scattering from deformed droplets and droplets with inclusions. II. Theoretical treatment. Appl Opt 2000;39(27):5031–9. doi:10.1364/Ao.39.005031.

[182] Videen G, Zubko E, Arnold JA, MacCall B, Weinberger AJ, Shkuratov Y, Muñoz O. On the interpolation of light-scattering responses from irregularly shaped particles. J Quant Spectrosc Radiat Transf 2018;211:123–8.

[183] Volten H, de Haan JF, Hovenier JW, Schreurs R, Vassen W, Dekker AG, Hoogenboom HJ, Charlton F, Wouts R. Laboratory measurements of angular distributions of light scattered by phytoplankton and silt. Limnol Oceonogr 1998;43:1180–97.

[184] Walters S, Zallie J, Seymour G, Pan YL, Videen G, Aptowicz KB. Characterizing the size and absorption of single nonspherical aerosol particles from angularly-resolved elastic light scattering. J Quant Spectrosc Radiat Transf 2019:439–44. doi:10.1016/j.jqsrt.2018.12.005.

[185] Wang C, Wen M, Bai L, Zhang T. Auto-classification for confocal back-scattering micro-spectrum at single-cell scale using principal component analysis. Optik (Stuttg) 2016;127:1007–10.

[186] Wang WJ, Wen YH, Lu JQ, Zhao L, Al-Qaysi SA, Hu XH. Rapid classification of micron-sized particles of sphere, cylinders and ellipsoids by diffraction image parameters combined with scattered light intensity. J Quant Spectrosc Radiat Transf 2019;224:453–9. doi:10.1016/j.jqsrt.2018.12.010.

[187] Wang YL, Chakrabarti A, Sorensen CM. A LS study of the scattering matrix elements of Arizona Road Dust. J Quant Spectrosc Radiat Transf 2015;163:72–9. doi:10.1016/j.jqsrt.2015.05.002.

[188] Waterman PC. Matrix formulation of electromagnetic scattering. Proceedings of the IEEE 1965;53(8):805–12. doi:10.1109/PROC.1965.4058.

[189] Wells KS, Beach DA, Keller D, Bustamante C. An analysis of circular intensity differential scattering measurements - studies on the sperm cell of Eledone-Cirrhosa. Biopolymers 1986;25(11):2043–64. doi:10.1002/bip.360251103.

[190] Wilkman, O. (2013). Miescatter. GitHub reposiroty. Retrieved from https://github.com/dronir/MieScatter.jl

[191] Wyatt PJ. Differential light scattering - a physical method for identifying living bacterial cells. Appl Opt 1968;7(10):1879. doi:10.1364/Ao.7.001879.

[192] Wyatt PJ, Phillips DT. Structure of single bacteria from LS. J Theor Biol 1972;37(3):493. doi:10.1016/0022-5193(72)90087-2.

[193] Wyatt PJ, Schehrer KL, Phillips SD, Jackson C, Chang YJ, Parker RG, Phillips DT, Bottiger JR. Aerosol-particle analyzer. Appl Opt 1988;27(2):217–21. doi:10.1364/Ao.27.000217.

[194] Yang H, Liu CX, Zhao XS, Sun YF, Hou ZB, Lv CF. Bioaerosols polarization measurement and identification by multi-wavelength near-distance lidar. 4th International Conference on Green Materials and Environmental Engineering (Gmee 2018); 2018.

[195] Yang P, Kattawar GW, Hong G, Minnis P, Hu YX. Uncertainties associated with the surface texture of ice particles in satellite-based retrieval of cirrus clouds - Part I: single-scattering properties of ice crystals with surface roughness. IEEE Trans Geosci Remote Sens 2008;46(7):1940–7. doi:10.1109/Tgrs.2008.916471.

[196] Yang P, Liou KN, Mishchenko MI, Gao B-C. Efficient finite-difference time-domain scheme for light scattering by dielectric particles: application to aerosols. Appl Opt 2000;39(21):3727–37. doi:10.1364/AO.39.003727.

[197] Yee K. Numerical solution of initial boundary value problems involving maxwell's equations in isotropic media. IEEE Trans Antennas Propag 1966;14(3):302–7. doi:10.1109/TAP.1966.1138693.

[198] Yurkin, M., & Hoekstra, A. (2014). *User manual for the discrete dipole approximation code ADDA* 1.3b4.

[199] Zhang JN, Bi L, Liu JP, Panetta RL, Yang P, Kattawar GW. Optical scattering simulation of ice particles with surface roughness modeled using the

Edwards-Wilkinson equation. J Quant Spectrosc Radiat Transf 2016;178:325–35. doi:10.1016/j.jqsrt.2016.02.013.

[200] Zubko E, Shkuratov Y, Hart M, Eversole J, Videen G. Backscattering and negative polarization of aggregate particles. Opt Lett 2003;28(17):1504–6. doi:10.1364/Ol.28.001504.

[201] Zubko E. Modeling light scattering by forsterite particles. J Quant Spectrosc Radiat Transf 2015;40:1204–7. doi:10.1364/OL.40.001204.

[202] Zubko E, Muinonen K, Munoz O, Nousiainen T, Shkuratov Y, Sun WB, Videen G. Light scattering by feldspar particles: comparison of model aggregate debris particles with laboratory samples. J Quant Spectrosc Radiat Transf 2013;131:175–87.